

# Kalman Filtering-Assisted Node Deployment for Distributed OTFS-ISAC: A Geometry-Aware Design for the Joint Sensing and Communication

Jyotsna Rani, *Student Member, IEEE*, Kuntal Deka, *Member, IEEE*, Ganesh Prasad, *Member, IEEE* and Zilong Liu, *Senior Member, IEEE*.

**Abstract**—Integrated sensing and communication (ISAC) has emerged as a key enabler for next-generation wireless networks, offering spectrum efficiency and reduced hardware complexity. While monostatic ISAC has been extensively investigated, its limited spatial diversity restricts reliability in high-mobility scenarios. Distributed ISAC mitigates this issue by leveraging cooperative nodes, yet conventional orthogonal frequency-division multiplexing (OFDM)-based designs remain highly sensitive to Doppler shifts and multipath fading. Recently, orthogonal time frequency space (OTFS) modulation has been introduced as a resilient alternative, as its delay-Doppler domain representation enables both robust communication and high-resolution sensing. Motivated by this, we extend OTFS modulation to distributed ISAC and investigate the critical but underexplored problem of spatial node deployment. We propose a triangulation-based framework that exploits spatial diversity to enhance target localization, velocity estimation, and achievable communication rates, and analytically establish the role of deployment geometry in minimizing estimation error. Furthermore, we integrate Kalman filtering (KF) into the distributed OTFS-ISAC framework to improve state tracking of moving targets, developing novel algorithms for active sensing, passive sensing, and joint sensing-communication. Closed-form analytical results are derived for localization error metrics under general topologies, and a near-optimal deployment strategy is identified by aligning receivers along orthogonal axes. Extensive numerical evaluations demonstrate that the proposed framework achieves significant reductions in localization error and bit error rate (BER), while effectively capturing the trade-offs between sensing accuracy and communication reliability. These contributions jointly highlight the potential of KF-assisted node placement in distributed OTFS-ISAC as a promising solution for reliable, high-performance operation in dynamic wireless environments.

**Index Terms**—Integrated sensing and communication, orthogonal time-frequency space modulation, distributed networks, Kalman filtering

## I. INTRODUCTION

The rapid advancement of vehicular networks toward autonomous and intelligent transportation has created unprecedented demands for technologies that can deliver both reliable communication and real-time sensing. Integrated Sensing and Communication (ISAC) has emerged as a promising solution

by unifying hardware and spectrum resources for simultaneous data transmission and environmental sensing. This joint design not only enhances spectral-efficiency but also simplifies the implementation [1]. Conventional waveforms like OFDM perform poorly in high-mobility vehicular environments. They are very sensitive to Doppler shifts and multipath fading. On the other hand, orthogonal time frequency space (OTFS) modulation maps information into the delay-Doppler domain, where the channel is more stable and sparse. Because of this, OTFS is well-suited for ISAC in vehicular networks. It allows high-resolution sensing and reliable communication even under strong mobility and multipath effects [2], [3]. However, using OTFS-based ISAC in vehicular networks is still challenging. The main issues are tracking moving vehicles, keeping communication reliable under strong Doppler, estimating the speeds of multiple targets, and achieving accurate localization in multipath conditions. The other challenge is in delivering wide coverage, high reliability, and fine sensing resolution with limited resources, which is difficult for a single centralized node. Large co-located antenna arrays can provide accuracy but come with high hardware and computational costs, specifically for the high processing OTFS signal. Distributed ISAC overcomes these issues by coordinating spatially separated low-complexity nodes, offering broad coverage, cooperative sensing, and robust communication while keeping per-node complexity low [4]. In this work, we consider the distributed OTFS-based ISAC along with the Kalman filtering (KF) to enhance the sensing and communication performance.

### A. Related Works

1) *Monostatic ISAC*: Monostatic ISAC systems operate with the transmitter and receiver located at the network node. This setup is widely studied because it can reduce hardware cost and improve spectrum efficiency by using the same waveform that serves both sensing and communication [5], [6]. Many works have applied OFDM-based monostatic ISAC together with MIMO arrays, showing that such systems can provide good range, angle, and velocity estimation [5], [7]. In vehicular environments, monostatic ISAC is desired since it is compact, cost-efficient, and compatible with current vehicle-to-everything (V2X) standards [6], [8]. However, the main drawback is that monostatic systems rely only on one observation point, which restricts spatial diversity and robustness. This limitation becomes more critical in high-mobility environments, where Doppler shifts and multipath effects reduce the

J. Rani and K. Deka are with the Department of Electronics & Electrical Engineering, Indian Institute of Technology Guwahati, India (e-mail: {r.jyotsna, kuntaldeka}@iitg.ac.in).

G. Prasad is with the Department of Electronics and Communication Engineering, National Institute of Technology Silchar, India (e-mail: gp-keskeshri@ece.nits.ac.in).

Z. Liu is with the School of Computer Science and Electronics Engineering, University of Essex, Colchester, UK (e-mail: zilong.liu@essex.ac.uk)

reliability of target tracking. Therefore, we need a distributed ISAC system to address these challenges.

2) *Distributed ISAC*: Distributed ISAC emerged as a promising approach to overcome the inherent limitations of monostatic systems by allowing multiple base stations, user devices, or vehicles to cooperate for ISAC. This cooperation increased spatial diversity and enhanced localization accuracy which were particularly important in high-mobility environments. Earlier works on uplink cooperative ISAC focused on waveform and resource allocation, showing that joint optimization could reduce the Cramér–Rao lower bound (CRLB) for sensing while ensuring communication quality [9]. In vehicular networks, cooperative time-division ISAC frameworks demonstrated that sharing sensing data among automated vehicles reduced detection errors and latency [10]. At the network level, distributed ISAC schemes based on coordinated multi-point (CoMP) transmission and multi-static radar reported scaling gains in sensing accuracy as the number of cooperating transceivers increased [11], [12]. Mutual information-based sensing metrics were also introduced to unify communication–sensing trade-offs, effectively modeling distributed ISAC as a virtual MIMO system [13]. Nevertheless, most of these designs relied on OFDM waveforms, which were sensitive to Doppler shifts and multipath effects, limiting their effectiveness in fast time-varying channels.

3) *OTFS-Based ISAC*: To overcome these limitations, recent studies increasingly focused on OTFS modulation as a resilient waveform for ISAC. Unlike OFDM, OTFS represents signals in the delay–Doppler (DD) domain that captures channel dynamics caused by scatterer geometry, which granted robustness against Doppler impairments and multipath fading in high-mobility settings such as vehicular networks. In [14], the quasi-static DD channels were used to infer communication states from sensing parameters, achieving reliable transmissions under dynamic conditions. Further, the authors in [15] advanced this study by formulating a DD-domain precoder that jointly minimizes BER under the constraint of transmit power and CRB that provided a fundamental interplay where higher sensing fidelity improved communication reliability. In [16], addressed practical resolution limits by introducing a low-complexity OMPFR algorithm for fractional delay-Doppler estimation. It enabled precise target profiling in monostatic OTFS-ISAC without excessive complexity. When extended to distributed settings, OTFS unlocked even greater performance gains by combining spatial diversity with DD-domain processing. In [17], power allocation strategies for CF-mMIMO OTFS-ISAC were designed which demonstrates the significant SINR and spectral efficiency improvements over OFDM. Further, authors in [18] developed sparse recovery-based association and localization methods for multistatic OTFS-ISAC, yielding scalable and bandwidth-efficient solutions for vehicular scenarios. On contrary, the work in [19] leveraged OTFS pilot sidelobes to achieve super-resolution range-velocity profiling, surpassing conventional time-bandwidth limits in automotive radar. Thus, the OTFS-enabled distributed ISAC achieves robust and scalable integration of communication and sensing. *However, the above works did not investigate the optimal location of the nodes in the distributed ISAC assisted*

*by the KF to enhance the sensing of the moving targets as well as the associated communications.*

## B. Motivation and Key Contributions

ISAC is becoming a key technology for next-generation wireless networks, offering spectrum efficiency and reduced hardware cost. Monostatic ISAC has been widely studied, but its reliance on a single observation point limits spatial diversity and makes it less reliable in high-mobility environments. Distributed ISAC addresses this issue through cooperation among multiple nodes, though most existing designs use OFDM, which is sensitive to Doppler shifts and multipath fading. OTFS modulation has recently been introduced as a more robust alternative, as its delay-Doppler domain representation provides resilience against time-varying channels and enables high-resolution sensing. Extending OTFS to distributed ISAC combines spatial diversity with delay-Doppler processing, yielding significant improvements in both sensing and communication. Despite these advances, prior research has mainly concentrated on waveform design and resource allocation, with little attention given to the optimal spatial deployment of nodes. Since node placement strongly impacts sensing coverage, localization accuracy, and communication quality in dynamic scenarios, this remains a critical but open problem. Furthermore, the temporal evolution of moving targets can be effectively tracked using KF, yet its integration with deployment optimization in distributed OTFS-ISAC has not been explored. These observations motivate our work on KF-assisted node placement strategies to enhance the joint performance of sensing and communication in distributed OTFS-ISAC systems. The key contributions of the work are listed below.

- We first introduce the topology of the distributed ISAC framework, describing the transmit OTFS waveform and the corresponding receive signal processing. We then present methods for active sensing and joint passive sensing and communications to estimate target range, radial velocity, and achievable data rate at the receivers. Based on the system topology, we propose a geometrical triangulation approach that exploits spatial diversity to improve the accuracy of target localization and velocity estimation. Using this spatial diversity, we describe two methods to improve the estimation of the location and velocity of the targets.
- Next, we establish a lemma that highlights the role of the triangulation area in reducing the localization error and show that optimizing this area is essential for an accurate estimation. A corollary then demonstrates that when receivers are placed along orthogonal axes, the estimation error can be minimized by maximizing the triangulation area. We further derive closed-form expressions for both the trace and the maximum eigenvalue of the covariance matrix of the estimated target locations under a general topology with randomly deployed receivers. Using these results, we prove in a subsequent lemma that a suboptimal yet effective topology is obtained when the receivers are positioned along orthogonal axes, which is

equivalent to a configuration of three nodes equipped with multiple independent antennas. Finally, we show that this equivalent topology reduces the estimation error by a factor proportional to the cubic power of the number of independent antennas per node.

- For moving vehicles, we employ KF to further improve the accuracy of state estimation. The underlying prediction model is derived from a continuous correlated random walk (CRW), which is then converted in the discrete-time domain for the tractable implementation. Based on this, we present a KF-based algorithm that estimates the dynamic states of the targets, specifically their position and velocity. Based on this, we extend the application of KF to develop a second algorithm aimed at enhancing active sensing performance by refining the prediction and correction steps. Furthermore, we propose a third algorithm that leverages KF for joint passive sensing and communication, thereby integrating tracking and information exchange within a unified scheme. Also, we conduct a thorough analysis of the time complexity of all three algorithms.
- To conclude, the effectiveness of the proposed framework is substantiated through an extensive set of numerical evaluations. The root mean square error (RMSE) is analyzed for both active and passive sensing modes to assess estimation accuracy. The incorporation of the KF is further shown to reduce the estimation error, thereby enhancing the reliability of the sensing process. In addition, while the passive sensing, we investigate the bit error rate (BER) performance when implementing ISAC, thereby providing deeper insights into the dual-function operation. To comprehensively assess the overall system behavior, a comparative numerical analysis across multiple schemes is conducted, highlighting the trade-offs, relative gains, and performance trends in both sensing and communication.

*Notations:* Throughout this paper, bold lowercase and uppercase letters denote column vectors and matrices, respectively. The set  $\mathbb{C}^{M \times N}$  represents all  $M \times N$  matrices with complex-valued entries. The operator  $\mathbb{E}\{\cdot\}$  denotes statistical expectation with respect to the underlying random variables. The Kronecker product of two matrices is denoted by  $\otimes$ . The operator  $\text{vec}(\cdot)$  stacks the columns of a matrix into a single column vector, whereas  $\text{vec}^{-1}(\cdot)$  performs the inverse mapping, reconstructing the matrix from its vectorized form. The notation  $\|\cdot\|$  represents the Euclidean norm of a vector. The operator  $\text{diag}\{\cdot\}$  generates a diagonal matrix with its diagonal entries specified by the argument.  $\mathcal{O}(\cdot)$  follows the conventional big-O notation to characterize asymptotic computational complexity.

## II. SYSTEM ARCHITECTURE

### A. Topology

As shown in Fig. 1, the system uses a distributed ISAC (Integrated Sensing and Communication) setup. It includes one anchor node (AN), called  $\mathcal{A}_0$ , and several receiver nodes  $\{\mathcal{R}_1, \dots, \mathcal{R}_Z\}$  placed in different locations. The system works

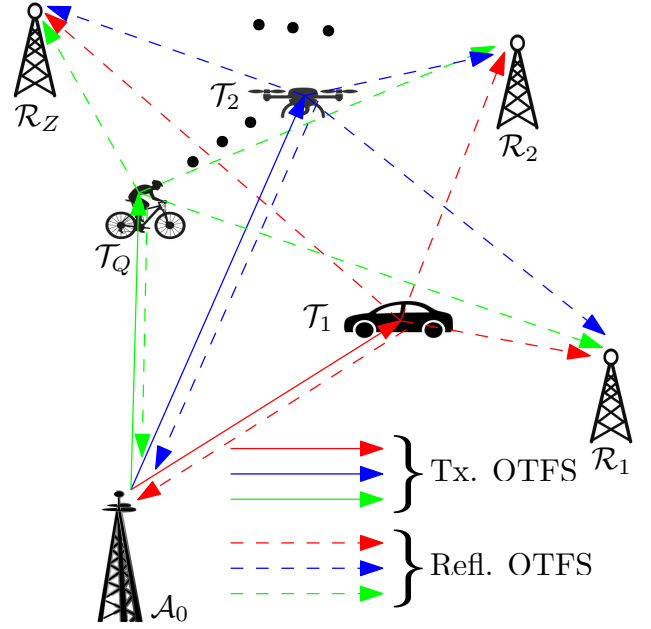


Fig. 1. Distributed network nodes for ISAC.

in two modes: active and passive sensing. In both modes, it uses monostatic and bistatic sensing. In monostatic sensing, the anchor node  $\mathcal{A}_0$  senses the environment using the echoes of its own signals reflected from the targets  $\{\mathcal{T}_1, \dots, \mathcal{T}_Q\}$ . In bistatic sensing, the anchor sends signals, and the receiver nodes  $\mathcal{R}_z; z \in \{1, \dots, Z\}$  collect the echoes reflected from the targets. This allows the anchor and receivers to work together as pairs. In active sensing mode, the anchor sends out known probing signals. These signals are also known to the receivers, so they can help with bistatic sensing. In passive sensing mode, the anchor sends normal communication signals to the receivers. The receivers use these signals to both decode information and sense the environment. They do this without sending out any signals themselves, which saves energy and avoids interference with the surroundings. Further, we consider the doubly spread channel; therefore, the transmit signal is modulated using OTFS which is described as follows.

### B. Transmit OTFS Signal

In OTFS signaling, an information data sequence, generated from the QAM alphabet  $\mathbb{A} \in \mathbb{C}$ , represented by the vector  $\mathbf{d}_I \in \mathbb{A}^{MN}$  is reshaped into a delay-Doppler domain matrix  $\mathbf{D}_I \in \mathbb{A}^{M \times N}$ . This transformation is carried out by dividing  $\mathbf{d}_I$  into  $N$  consecutive segments of length  $M$ , with each segment forming one column of the matrix  $\mathbf{D}_I$ . The parameters  $M$  and  $N$  correspond to the number of delay and Doppler bins, respectively. To facilitate integrated sensing and communication (ISAC), a pilot matrix  $\mathbf{D}_P \in \mathbb{C}^{M \times N}$  is introduced along with the data matrix. The indices for the delay and Doppler bins in both  $\mathbf{D}_I$  and  $\mathbf{D}_P$  are denoted by  $l \in \{0, \dots, M-1\}$  and  $k \in \{0, \dots, N-1\}$ , respectively. Note that the total bandwidth and duration of the OTFS signal is  $M\Delta f$  and  $NT$ , where  $T\Delta f = 1$ . Therefore, the resolutions of the delay and

Doppler shift are  $1/M\Delta f$  and  $1/NT$ . Further, the indices  $l$  and  $k$  provide the delay  $l/M\Delta f$  and Doppler shift  $k/NT$ . The pilot matrix  $\mathbf{D}_P$  is designed to have a single nonzero entry at the location  $(l_p, k_p)$ , i.e.,  $\mathbf{D}_P(l, k) = \sqrt{MN\sigma_P^2}$  if  $(l, k) = (l_p, k_p)$ , and zero elsewhere. This ensures that the average pilot power is maintained as  $\mathbb{E}\{|\mathbf{D}_P(l, k)|^2\} = \sigma_P^2$ . The resultant data ISAC is given by  $\mathbf{D} = \mathbf{D}_I + \mathbf{D}_P$ . Next, this delay-Doppler data is converted into the time-frequency domain using a mathematical operation called the Inverse Symplectic Finite Fourier Transform (ISFFT). This is done by multiplying the data with two Fourier transform matrices:  $\mathbf{X} = \mathbf{F}_M \mathbf{D} \mathbf{F}_N^H$ . Here,  $\mathbf{F}_M$  and  $\mathbf{F}_N$  are standard Fast Fourier Transform (FFT) matrices, and the superscript  $H$  means we are using the inverse FFT (also called Hermitian transpose). Thereafter, the time-frequency signal is converted to the time domain using an inverse FFT, and then passed through a pulse-shaping filter  $p(t)$  of duration  $T$  which is denoted in diagonal matrix form as  $\mathbf{P}_{tx} = \text{diag}\{p_{tx}(0), p_{tx}(1), \dots, p_{tx}(M-1)\}$  using its samples. This filter helps to shape the signal for better transmission through the wireless channel. Thus the OTFS transmit signal  $\mathbf{S}$  is:

$$\mathbf{S} = \mathbf{P}_{tx} \mathbf{F}_M^H (\mathbf{F}_M \mathbf{D} \mathbf{F}_N^H) \mathbf{s}, \quad (1)$$

Further, the resulting time-domain signal vector  $\mathbf{s} \in \mathbb{C}^{MN \times 1}$  is obtained by stacking the columns of  $\mathbf{S}$  as:

$$\mathbf{s} = (\mathbf{F}_N^H \otimes \mathbf{P}_{tx}) \mathbf{d}, \quad (2)$$

where the vector  $\mathbf{d} = \text{vec}(\mathbf{D}) \in \mathbb{C}^{MN \times 1}$ , formed by stacking the columns of  $\mathbf{D}$ . This process allows the transmitter to send signals that are more robust to motion and reflections, making OTFS a good fit for environments with both sensing and communication.

### C. Received Signal Processing

In doubly-dispersive channel, the received signal  $\mathbf{r}_j$  at the  $j$ th receiver is the superposition of the signals via the  $P$  paths, where each path introduces a gain, cyclic delay, and Doppler shift. The channel matrix  $\mathbf{H}_j$  for the  $j$ th receiver is given by:

$$\mathbf{H}_j = \sum_{q=1}^P h_{q,j} \mathbf{\Pi}^{l_{q,j}} \mathbf{\Delta}^{k_{q,j}}. \quad (3)$$

Here,  $h_{q,j}$  is the channel coefficient and  $l_{q,j}$ ,  $k_{q,j}$  are the indices of the delay and Doppler shift of the  $q$ th path.  $\mathbf{\Pi}^{l_{q,j}}$  is  $l_{q,j}$ -step forward cyclic shift to the permutation matrix  $\mathbf{\Pi}$  as given in [20, eq. (9)]. This parameter gives  $l_{q,j}$ -step cyclic shift to the transmit signal  $\mathbf{s}$  in the  $q$ th path. On the other hand  $\mathbf{\Delta}^{k_{q,j}}$  gives the Doppler shift by frequency  $2\pi k_{q,j}/MN$ , where  $\mathbf{\Delta} = \text{diag}\{c^0, c^1, \dots, c^{MN-1}\}$ , where  $c = e^{i2\pi/MN}$ . Here both the matrices  $\mathbf{\Pi}$  and  $\mathbf{\Delta}$  are of size  $MN \times MN$ . Using (3), the received signal  $\mathbf{r}_j$  is expressed as:

$$\mathbf{r}_j = \mathbf{H}_j \mathbf{s} + \mathbf{n}_j, \quad (4)$$

where  $\mathbf{n}_j \in \mathcal{CN}(\mathbf{0}, \sigma_j^2 \mathbf{I}_{MN})$ .

In order to perform the sensing and communication using the received signal  $\mathbf{r}_j$ , we first represent it from the time domain to delay-Doppler using the inverse process of obtaining  $\mathbf{s}$  from  $\mathbf{d}$  (cf. (2)), which is described as follows. The time domain signal in matrix form is obtained as:

$\mathbf{R}_j = \text{vec}^{-1}(\mathbf{r}_j)$ . Then, it is passed through a receiver filter  $\mathbf{P}_{rx} = \text{diag}\{p_{rx}(0), p_{rx}(1), \dots, p_{rx}(M-1)\}$  which is generated using sampling of pulse-shaping waveform  $p_{rx}(t)$  at the receiver. Then, delay-Doppler domain signal  $\mathbf{Y}_j$  is obtained by performing  $M$ -point FFT followed by SFFT on it which is represented as:  $\mathbf{Y}_j = \mathbf{F}_M^H (\mathbf{F}_M \mathbf{P}_{rx} \mathbf{R}_j) \mathbf{F}_N = \mathbf{P}_{rx} \mathbf{R}_j \mathbf{F}_N$ . The corresponding vector  $\mathbf{y}_j$  is obtained as:

$$\mathbf{y}_j = (\mathbf{F}_N \otimes \mathbf{P}_{rx}) \mathbf{r}_j \quad (5a)$$

$$= \overline{\mathbf{H}}_j \mathbf{d} + \overline{\mathbf{n}}_j, \quad (5b)$$

where (5b) is obtained from (5a) by substituting  $\mathbf{r}_j$ ,  $\mathbf{s}$ , and  $\mathbf{H}_j$  from (4), (2), and (3). Thus,  $\overline{\mathbf{H}}_j = \sum_{q=1}^P h_{q,j} \mathcal{T}(l_{q,j}, k_{q,j})$  and  $\mathcal{T}(l_{q,j}, k_{q,j}) = (\mathbf{F}_N \otimes \mathbf{P}_{rx}) \mathbf{\Pi}^{l_{q,j}} \mathbf{\Delta}^{k_{q,j}} (\mathbf{F}_M^H \otimes \mathbf{P}_{tx})$ . Note that  $\mathbf{P}_{tx} = \mathbf{P}_{rx} = \mathbf{I}_M$  for rectangular pulse-shaping filter. The noise  $\overline{\mathbf{n}}_j = (\mathbf{F}_N \otimes \mathbf{P}_{rx}) \mathbf{n}_j$  and it can be shown that it follows the Gaussian distribution  $\overline{\mathbf{n}}_j \in \mathcal{CN}(\mathbf{0}, \sigma_j^2 \mathbf{I}_{MN})$  for the normalized unitary matrix  $\mathbf{F}_N$ .

### D. Active Sensing

In active sensing, the transmit data vector  $\mathbf{d}$  is assumed to be known at all receiving nodes. Utilizing this prior knowledge, the range and radial velocity of targets relative to the  $j$ th receiver can be determined by estimating the set of parameters  $h_j$ ,  $\tau_j$ , and  $\nu_j$ , which represent the complex gains, propagation delays, and Doppler shifts, respectively.

These parameters are obtained by solving a maximum likelihood estimation problem. Under the assumption of additive Gaussian noise at the receivers, the log-likelihood function simplifies to a least-squares minimization problem, where the received delay-Doppler vector  $\mathbf{y}_j$  is compared with its expected value  $\overline{\mathbf{H}}_j \mathbf{d}$ . This leads to the following estimator formulation:

$$(\hat{\mathbf{h}}_j, \hat{\tau}_j, \hat{\nu}_j) = \arg \min_{(\mathbf{h}_j, \tau_j, \nu_j)} \left\| \mathbf{y}_j - \sum_{q=1}^P h_{q,j} \mathcal{T}(\tau_{q,j}, \nu_{q,j}) \mathbf{d} \right\|^2, \quad (6)$$

where  $\mathcal{T}(\tau_{q,j}, \nu_{q,j})$  denotes the combined delay and Doppler shift operator acting on the transmit signal. The problem in (6) is nonconvex due to the discrete nature of the delay and Doppler parameters and is computationally intensive because the search space spans the high-dimensional domain  $\mathbb{C}^P \times \mathbb{R}_+^P \times \mathbb{R}^P$ . To mitigate this complexity, we adopt a sequential estimation strategy. In the first step, the parameters of the dominant path delay  $\tau_{1,j}$  and Doppler shift  $\nu_{1,j}$  are obtained by maximizing the correlation between the received signal and the delayed-Doppler shifted transmit waveform:

$$(\hat{\tau}_{1,j}, \hat{\nu}_{1,j}) = \arg \max_{(\tau_{1,j}, \nu_{1,j})} \left| (\mathcal{T}(\tau_{1,j}, \nu_{1,j}) \mathbf{d})^H \mathbf{y}_j \right|^2. \quad (7)$$

Given  $(\hat{\tau}_{1,j}, \hat{\nu}_{1,j})$ , the corresponding complex gain  $h_{1,j}$  is estimated by minimizing the residual error with respect to  $h_{1,j}$ , which leads to a closed-form expression:

$$\hat{h}_{1,j} = \frac{(\mathcal{T}(\hat{\tau}_{1,j}, \hat{\nu}_{1,j}) \mathbf{d})^H \mathbf{y}_j}{\mathbf{d}^H \mathcal{T}(\hat{\tau}_{1,j}, \hat{\nu}_{1,j})^H \mathcal{T}(\hat{\tau}_{1,j}, \hat{\nu}_{1,j}) \mathbf{d}}. \quad (8)$$

Subsequent paths are estimated successively. For the estimation of the  $i$ th path parameters, the contribution from previously estimated paths is subtracted from the received signal,

and the same correlation-maximization and gain estimation procedure is applied:

$$(\hat{\tau}_{i,j}, \hat{\nu}_{i,j}) = \arg \max_{(\tau_{i,j}, \nu_{i,j})} |(\mathcal{T}(\tau_{i,j}, \nu_{i,j})\mathbf{d})^H \mathbf{y}_j| \quad (9a)$$

$$\begin{aligned} & - \left| \sum_{q=1}^{i-1} \hat{h}_{q,j} \mathcal{T}(\hat{\tau}_{q,j}, \hat{\nu}_{q,j})\mathbf{d} \right|^2 \\ \hat{h}_{i,j} &= \frac{(\mathcal{T}(\hat{\tau}_{i,j}, \hat{\nu}_{i,j})\mathbf{d})^H \mathbf{y}_j}{\mathbf{d}^H \mathcal{T}(\hat{\tau}_{i,j}, \hat{\nu}_{i,j})^H \mathcal{T}(\hat{\tau}_{i,j}, \hat{\nu}_{i,j})\mathbf{d}} \end{aligned} \quad (9b)$$

*Complexity:* The computational cost of the sequential estimator is dominated by the two-dimensional delay-Doppler correlation search. For each delay-Doppler pair, the correlation involves an inner product of length  $MN$  that gives the complexity of  $\mathcal{O}(G_\tau G_\nu MN)$  per path at a single receiver, where  $G_\tau$  and  $G_\nu$  denote the grid sizes in delay and Doppler, respectively. The gain estimation step requires only a few additional inner products of length  $MN$ , i.e.,  $\mathcal{O}(MN)$ , and is negligible compared with the search stage. Repeating the procedure for  $P$  paths results in a per-receiver complexity of  $\mathcal{O}(PG_\tau G_\nu MN)$ . Considering all  $Z+1$  receivers, the overall complexity is  $\mathcal{O}((Z+1)PG_\tau G_\nu MN)$ . Thus, the overall complexity grows linearly with the number of paths, the signal dimension, and the number of receivers, but quadratically with the resolution of the delay-Doppler grid, with the correlation search being the dominant factor.

Now, using the estimated delay and Doppler shift vectors  $\hat{\tau}_j$  and  $\hat{\nu}_j$  at the  $j$ th receiver, we can determine the range and radial velocities of the  $P$  targets. The receiver  $\mathcal{A}_0$  (for  $j=0$ ) gets the self-reflected signal, the range  $\rho_{i,0}$  and the radial velocity  $v_{i,0}$  of the  $i$ th target can be computed as in (10a) below. Whereas, for receivers  $j \in \{1, \dots, Z\}$ , the range  $\rho_{i,j}$  and radial velocity  $v_{i,j}$  of the  $i$ th target are given in (10b).

$$\hat{\rho}_{i,0} = \hat{\tau}_{i,0}c/2; \quad \hat{v}_{i,0} = \hat{\nu}_{i,0}c/2f_c, \quad (10a)$$

$$\hat{\rho}_{i,j} = \hat{\tau}_{i,j}c - \hat{\rho}_{i,0}; \quad \hat{v}_{i,j} = (\hat{\nu}_{i,j} - \hat{\nu}_{i,0})c/f_c. \quad (10b)$$

### E. Joint Passive Sensing and Communication

In this scenario, only the pilot signal is assumed to be known at all receivers. Consequently, the channel—characterized by its gain, delay, and Doppler shift components—is first estimated. Based on this initial channel estimate, the information data is subsequently detected. Utilizing both the estimated data and the known pilot signal, the channel is re-estimated in the next iteration. This iterative process continues until convergence is achieved. For an initial (coarse) estimate of the channel, the delay-Doppler matrix of the pilot signal, denoted as  $\mathbf{D}_P$ , is vectorized as  $\mathbf{d}_P = \text{vec}\mathbf{D}_P$ . Using this representation, each receiver estimates the channel while treating the transmitted information data  $\mathbf{d}_I$  as interference. Analogous to (6), the channel coarse estimator at the  $j$ -th receiver is expressed as:

$$(\hat{\mathbf{h}}_j^{(0)}, \hat{\tau}_j^{(0)}, \hat{\nu}_j^{(0)}) = \arg \min_{(\mathbf{h}_j, \tau_j, \nu_j)} \left\| \mathbf{y}_j - \sum_{q=1}^P h_{q,j} \mathcal{T}(\tau_{q,j}, \nu_{q,j})\mathbf{d}_P \right\|^2, \quad (11)$$

The problem in (11) can be solved using the sequential estimation strategy as described in (7), (8), and (9). However, this initial coarse estimation is inherently less accurate than in the active sensing scenario, where both the pilot signal  $\mathbf{d}_P$  and the information data  $\mathbf{d}_I$  are known to all receivers. To improve estimation accuracy in this passive setting, we adopt an iterative refinement algorithm as outlined below. Starting with the coarse channel estimate  $(\hat{\mathbf{h}}_j^{(0)}, \hat{\tau}_j^{(0)}, \hat{\nu}_j^{(0)})$ , the information data is recovered using a channel equalizer. This step is formulated as a regularized least-squares optimization problem:

$$\min_{\mathbf{d}} \|\mathbf{y}_j - \bar{\mathbf{H}}_j \mathbf{d}\|^2 + \mu \|\mathbf{d}\|^2, \quad (12)$$

where  $\mu$  is a regularization parameter that ensures numerical stability, especially when the estimated channel matrix  $\bar{\mathbf{H}}_j$  is ill-conditioned or rank-deficient. Without regularization, a nearly singular  $\bar{\mathbf{H}}_j$  can lead to solutions that are overly sensitive to noise, resulting in overfitting. The regularization term  $\mu\|\mathbf{d}\|^2$  mitigates this effect by penalizing large values in the solution, effectively reducing the bias toward noise-induced errors. Based on the minimum mean square error (MMSE), the closed-form solution to (12) is given by:

$$\hat{\mathbf{d}}_{\text{MMSE}} = (\bar{\mathbf{H}}_j^H \bar{\mathbf{H}}_j + \mu \mathbf{I})^{-1} \bar{\mathbf{H}}_j^H \mathbf{y}_j. \quad (13)$$

However, for the large channel matrix  $\bar{\mathbf{H}}_j$ , it is complex to solve using (13) due to the computation of the matrix inverse. Therefore, we consider gradient descent-based iterative method where the gradient  $\nabla J(\mathbf{d})$  in  $t$ th iteration and the update rule for  $(t+1)$ th iteration are given below in (14a) and (14b).

$$\nabla J(\mathbf{d})^{(t)} = 2\bar{\mathbf{H}}_j^H (\bar{\mathbf{H}}_j \mathbf{d}^{(t)} - \mathbf{y}_j) + 2\mu \mathbf{d}^{(t)}, \quad (14a)$$

$$\mathbf{d}^{(t+1)} = \mathbf{d}^{(t)} - \eta \nabla J(\mathbf{d})^{(t)}, \quad (14b)$$

Here,  $\eta$  denotes the step size used in the gradient descent updates. The inner-loop iteration for data estimation continues until convergence which is defined by the stopping criterion:  $\|\mathbf{d}^{(t+1)} - \mathbf{d}^{(t)}\| < \epsilon$ , where  $\epsilon$  is a pre-defined threshold that controls the convergence precision. Once the convergence is achieved and the final estimate of the data vector is obtained as  $\mathbf{d}'$ , it is transformed back into the delay-Doppler domain via inverse vectorization:  $\mathbf{D}' = \text{vec}^{-1}(\mathbf{d}')$ . Subsequently, the estimated information component in the delay-Doppler domain is extracted by subtracting the known pilot matrix:  $\mathbf{D}'_I = \mathbf{D}' - \mathbf{D}_P$ . To recover the transmitted information symbols, a symbol-wise demodulation is performed. Specifically, the final estimate of the information data  $\hat{\mathbf{D}}_I$  is obtained by solving the following nearest neighbor projection problem:

$$\hat{\mathbf{D}}_I = \arg \min_{\mathbf{D}_I \in \mathbb{A}^{M \times N}} \|\mathbf{D}'_I - \mathbf{D}'_I\|^2, \quad (15)$$

where  $\mathbb{A}$  denotes the QAM modulation alphabet. With both the pilot  $\mathbf{D}_P$  and the newly estimated information data  $\hat{\mathbf{D}}_I$  now available at the receiver, a refined channel estimation can be carried out using the active sensing framework described in Section II-D. In this stage, the full delay-Doppler matrix  $\hat{\mathbf{D}} = \hat{\mathbf{D}}_I + \mathbf{D}_P$  is treated as known input. Following the updated channel estimate, the information data is re-estimated using the same regularized MMSE method approximation, leveraging the improved channel knowledge. This forms the

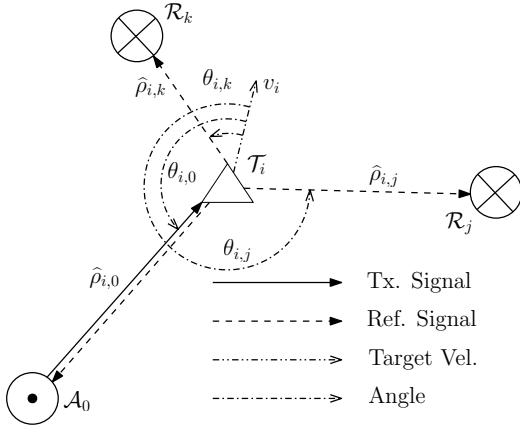


Fig. 2. Estimation of location and velocity of a target via cooperative sensing.

basis of an *outer-loop iteration*, wherein the data and channel estimates are refined alternately. The process continues until convergence is achieved, ensuring that both the channel parameters and information data are jointly optimized in a passive sensing and communication. Note that the above method for the joint passive sensing and communication is used at all the  $Z$  receivers. Further, using the estimated channel parameters, the distance and radial velocities of the targets to the receivers can be calculated using (10)<sup>1</sup>. Next, we determine the location and velocity of a target using its estimated ranges and velocities to the  $Z + 1$  receivers.

### III. TARGETS LOCALIZATION VIA COOPERATIVE SENSING

This section presents a method for determining the location and velocity of a target and then improving accuracy using the estimated ranges and radial velocities relative to the AN  $\mathcal{A}_0$  and a set of spatially separated receivers.

#### A. Targets' Location

As illustrated in Fig. 2, the location a target  $\mathcal{T}_i$  is estimated using geometric triangulation formed by the transmitter  $\mathcal{A}_0$  and two distinct receivers  $\mathcal{R}_j$  and  $\mathcal{R}_k$ , where  $j, k \in \{1, \dots, Z\}$  and  $j \neq k$ . The estimated ranges  $\hat{\rho}_{i,0}$ ,  $\hat{\rho}_{i,j}$ , and  $\hat{\rho}_{i,k}$  from the target to each of these three nodes are computed based on the estimation procedure described in (10). Given the known positions of the transmitter and receivers, namely  $(x_0, y_0)$  for  $\mathcal{A}_0$ , and  $(x_j, y_j)$ ,  $(x_k, y_k)$  for  $\mathcal{R}_j$  and  $\mathcal{R}_k$ , respectively, the position  $(\alpha_i, \beta_i)$  of the  $i$ th target can be determined as follows. First, the Euclidean distance equations from the target to each of the three nodes are expressed as in (16a). Further, by subtracting the equations corresponding to  $q = j$  and  $q = k$  from the equation for  $q = 0$ , we obtain two simplified linear equations in (16b). Further, these are represented in matrix form in (16c).

$$(x_q - \alpha_i)^2 + (y_q - \beta_i)^2 = \rho_{i,q}^2; \quad q \in \{0, j, k\} \quad (16a)$$

$$\begin{bmatrix} x_q - x_0 & y_q - y_0 \end{bmatrix} \begin{bmatrix} \alpha_i \\ \beta_i \end{bmatrix} = \frac{1}{2}(\rho_{i,0}^2 - \rho_{i,q}^2)$$

$$- (x_0^2 - x_q^2) - (y_0^2 - y_q^2); \quad q \in \{j, k\} \quad (16b)$$

$$\mathbf{A} \begin{bmatrix} \alpha_i \\ \beta_i \end{bmatrix} = \mathbf{B}; \quad \mathbf{A} = \begin{bmatrix} x_j - x_0 & y_j - y_0 \\ x_k - x_0 & y_k - y_0 \end{bmatrix}$$

$$\mathbf{B} = \frac{1}{2} \begin{bmatrix} \rho_{i,0}^2 - \rho_{i,j}^2 - (x_0^2 - x_j^2) - (y_0^2 - y_j^2) \\ \rho_{i,0}^2 - \rho_{i,k}^2 - (x_0^2 - x_k^2) - (y_0^2 - y_k^2) \end{bmatrix} \quad (16c)$$

$$\begin{bmatrix} \alpha_i \\ \beta_i \end{bmatrix} = \mathbf{A}^{-1} \mathbf{B} \quad (16d)$$

The solution in (16d) uniquely determines the location of the  $i$ th target provided that the matrix  $\mathbf{A}$  is full rank, which holds true when the transmitter and the two receivers are not collinear.

#### B. Targets' Velocity

Using geometric triangulation, as illustrated in Fig. 2, we also estimate the velocity of the target. To do so, we first define the unit vectors  $\{\mathbf{u}_{q,i}\}$  from the  $i$ th target to the two observing nodes  $q \in \{j, k\}$ . These are given by:  $\mathbf{u}_{q,i} = [(x_q - \alpha_i)/\rho_{i,q}, (y_q - \beta_i)/\rho_{i,q}]^T$ , where  $(x_q, y_q)$  denotes the coordinates of node  $q$ , and  $\rho_{i,q}$  is the Euclidean distance between the target and node  $q$ . Let the unknown velocity of the  $i$ th target be  $\mathbf{v}_i = [v_{i,x}, v_{i,y}]^T$ , where  $v_{i,x}$  and  $v_{i,y}$  are its components along the  $x$  and  $y$  axes, respectively. The projection of  $\mathbf{v}_i$  onto the unit vector  $\mathbf{u}_{q,i}$  yields the radial velocity measured by node  $q$ , denoted as  $v_{i,q}$ . This can be expressed as:  $v_{i,q} = \mathbf{v}_i^T \mathbf{u}_{q,i}$ ,  $q \in \{j, k\}$ . By arranging these equations in matrix form, we obtain a linear system:

$$\mathbf{C} \begin{bmatrix} v_{i,x} \\ v_{i,y} \end{bmatrix} = \mathbf{D} \Rightarrow \begin{bmatrix} v_{i,x} \\ v_{i,y} \end{bmatrix} = \mathbf{C}^{-1} \mathbf{D};$$

$$\mathbf{C} = \begin{bmatrix} (x_j - \alpha_i)/\rho_{i,j} & (y_j - \beta_i)/\rho_{i,j} \\ (x_k - \alpha_i)/\rho_{i,k} & (y_k - \beta_i)/\rho_{i,k} \end{bmatrix}, \quad \mathbf{D} = \begin{bmatrix} v_{i,j} \\ v_{i,k} \end{bmatrix} \quad (17)$$

This system yields the solution for the velocity vector  $\mathbf{v}_i$ , assuming  $\mathbf{C}$  is invertible, which is generally ensured by appropriate geometric placement of the nodes. Given  $Z$  receivers, a total of  $\mathcal{Z} \triangleq \binom{Z}{2}$  unique receiver pairs can be formed in conjunction with  $\mathcal{A}_0$  to construct geometric triangles. Each of these  $\mathcal{Z}$  configurations provides an independent estimate of a target's location and velocity using (16d) and (17). The straightforward approach to reduce estimation error is to compute the arithmetic mean of the location and velocity estimates obtained from all  $\mathcal{Z}$  triangle configurations. The averaged location and velocity of the  $i$ th target are given by:

$$(\alpha_{i,\text{avg}}, \beta_{i,\text{avg}}) = \left( \frac{1}{\mathcal{Z}} \sum_{t=1}^{\mathcal{Z}} \alpha_{i,t}, \frac{1}{\mathcal{Z}} \sum_{t=1}^{\mathcal{Z}} \beta_{i,t} \right), \quad (18a)$$

$$(v_{i,x,\text{avg}}, v_{i,y,\text{avg}}) = \left( \frac{1}{\mathcal{Z}} \sum_{t=1}^{\mathcal{Z}} v_{i,x,t}, \frac{1}{\mathcal{Z}} \sum_{t=1}^{\mathcal{Z}} v_{i,y,t} \right) \quad (18b)$$

While this approach can mitigate random noise and improve robustness, it does not account for the fact that certain triangle configurations may introduce significantly higher errors due to unfavorable geometric conditions, e.g., near-collinear arrangements or poor baseline separations. To further enhance the estimation accuracy by leveraging the multiple geometric configurations, we next introduce a selection based approach that selectively utilizes only the most reliable component estimates.

<sup>1</sup>The computational complexity of the passive sensing and communication approach is investigated later while the discussion of Algorithm 3.

### C. Nearest-Neighbor-Based Selection Approach

Averaging across all  $Z$  triangle-based estimates can help suppress random noise, but it does not consider the reliability of each configuration. In practice, some triangles may yield highly inaccurate estimates due to poor geometry, for example, when nodes are nearly collinear or too closely spaced. To address this, we propose a *nearest-neighbor selection method* that prioritizes consistency among estimates. Let the set of location or velocity estimates for the  $i$ th target be represented by  $\mathcal{C} = \{C_1, C_2, \dots, C_Z\}$ , where each  $C_t \in \mathbb{R}^2$  corresponds to either  $[\alpha_{i,t}, \beta_{i,t}]^T$  or  $[v_{i,x,t}, v_{i,y,t}]^T$ . To identify the most coherent subset of estimates, we calculate the Euclidean distance between each pair of points in  $\mathcal{C}$ . For a predefined threshold  $\xi > 0$ , the neighbor set  $\mathcal{S}_n$  of an estimate  $C_n$  includes all other estimates that lie within distance  $\xi$  of it:

$$\mathcal{S}_n = \{C_m \in \mathcal{C} \setminus \{C_n\} \mid \|C_n - C_m\| \leq \xi\} \quad (19)$$

Among all such sets, we identify the one with the largest number of neighbors:

$$n^* = \arg \max_n |\mathcal{S}_n| \quad (20)$$

where  $|\cdot|$  denotes the number of elements in a set. The final estimate is then computed by averaging  $C_{n^*}$  with all points in its neighbor set:

$$C_{\text{avg}} = \frac{1}{|\mathcal{S}_{n^*}| + 1} \left( C_{n^*} + \sum_{C_m \in \mathcal{S}_{n^*}} C_m \right) \quad (21)$$

By selecting and averaging only those estimates that exhibit spatial coherence, this method reduces the influence of unexpected estimates with large errors. Next, we investigate the effect of the locations of the AN  $\mathcal{A}_0$  and receivers in geometrical triangulation while estimating the location of the targets.

### D. Channel Estimation Using Sensing

After enhancing the sensing using the above methods, using the estimated location  $\{\hat{\alpha}_i, \hat{\beta}_i\}$  and velocity  $\{v_{i,x}, v_{i,y}\}$  of the  $P$  targets, the double-spread channel can be realized back as follows. As the location of the AN and receivers is known, the delay of the channels can be realized as:

$$\hat{\tau}_{i,0} = 2\hat{\rho}_{i,0}/c, \quad \hat{\tau}_{i,j} = (\hat{\rho}_{i,j} + \hat{\rho}_{i,0})/c; \quad \text{for } j \in \{1, \dots, Z\} \quad (22)$$

where  $\hat{\rho}_{i,j} = \sqrt{(\hat{\alpha}_{i,j} - x_j)^2 + (\hat{\beta}_{i,j} - y_j)^2}$  for  $j \in \{0, 1, \dots, Z\}$ . To determine the Doppler shift using the estimated velocity of the targets, first, we obtain the radial unit vector from the AN and receivers to the targets as:  $\mathbf{u}_{i,j} = [(\hat{\alpha}_i - x_j), (\hat{\beta}_i - y_j)]^T / \hat{\rho}_{i,j}$ . Using it, the radial velocity  $\hat{v}_{i,j}$  is determined by:  $\hat{v}_{i,j} = \hat{\mathbf{v}}_i^T \mathbf{u}_{i,j}$ , where  $\hat{\mathbf{v}}_i = [\hat{v}_{i,x}, \hat{v}_{i,y}]^T$ . Now, using the estimated radial velocities, the Doppler shifts are estimated as:

$$\hat{v}_{i,0} = 2\hat{v}_{i,0} f_c / c, \quad \hat{v}_{i,j} = \hat{v}_{i,j} f_c / c + \hat{v}_{i,0}; \quad \text{for } j \in \{1, \dots, Z\} \quad (23)$$

Using the estimated delay  $\hat{\tau}_{i,j}$  and Doppler shift  $\hat{v}_{i,j}$ , the channel gain  $\hat{h}_{i,j}$  can be determined using (9b).

### E. Desired Locations of the AN and the Receivers

Using Fig. 2, we investigate the effect of the location of the AN and receivers on the estimation of the location of the targets using the following lemma.

**Lemma 1.** *For the given variances,  $\{\sigma_{i,q}^2\}$ ;  $q \in \{0, j, k\}$  in the estimation of the square of the ranges of the  $i$ th target from the nodes,  $\mathcal{A}_0$ ,  $\mathcal{R}_j$ , and  $\mathcal{R}_k$ , the  $\text{tr}(\text{cov}(\hat{\alpha}_i, \hat{\beta}_i))$  or  $\kappa_{\max}(\text{cov}(\hat{\alpha}_i, \hat{\beta}_i))$  of the estimated location  $(\hat{\alpha}_i, \hat{\beta}_i)$  using geometrical triangulation (cf. Fig. 2), can be minimized by optimizing the magnitude of the area of the triangle formed using the three nodes.*

*Proof.* Without loss of generality, for simplicity, we assume that the AN  $\mathcal{A}_0$  is placed at the origin, i.e., its coordinate is  $(0, 0)$  and the coordinates of  $\mathcal{R}_j$  and  $\mathcal{R}_k$  are  $(x_j, y_j)$  and  $(x_k, y_k)$ . Using (16a), it can be shown that for given  $\{\sigma_{i,q}^2\}$ ;  $q \in \{0, j, k\}$ , the variances  $\sigma_{\alpha_i}^2$  and  $\sigma_{\beta_i}^2$  in the estimation of the x and y coordinates of the location of the  $i$ th target using the geometrical triangulation in Fig. 2, is given by:

$$\sigma_{\gamma_i}^2 = \frac{\sigma_{i,j}^2 (g_j + g_k)^2 + \sigma_{i,0}^2 g_k^2 + \sigma_{i,k}^2 g_j^2}{\mathcal{D}},$$

where  $\gamma = \alpha$ ; for  $g = y$ ,  $\gamma = \beta$ ; for  $g = x$ , and  $\mathcal{D} = (x_j y_k - x_k y_j)^2$ . We assume that the errors in the estimation of  $\hat{\alpha}_i$  and  $\hat{\beta}_i$  are independent of each other. Therefore, the covariance matrix  $\text{cov}(\hat{\alpha}_i, \hat{\beta}_i)$  is diagonal matrix. Thus,  $\text{tr}(\text{cov}(\hat{\alpha}_i, \hat{\beta}_i))$  and  $\kappa_{\max}(\text{cov}(\hat{\alpha}_i, \hat{\beta}_i))$  are expressed as:

$$\text{tr}(\text{cov}(\hat{\alpha}_i, \hat{\beta}_i)) = \sigma_{\alpha_i}^2 + \sigma_{\beta_i}^2 = \sigma_{i,j}^2 [(x_j + x_k)^2 + (y_j + y_k)^2] + \sigma_{i,0}^2 [x_k^2 + y_k^2] + \sigma_{i,k}^2 [x_j^2 + y_j^2] / (x_j y_k - x_k y_j)^2 \quad (24a)$$

$$\kappa_{\max}(\text{cov}(\hat{\alpha}_i, \hat{\beta}_i)) = \frac{1}{(x_j y_k - x_k y_j)^2} \max\{\sigma_{i,j}^2 (x_j + x_k)^2 + \sigma_{i,0}^2 x_k^2 + \sigma_{i,k}^2 x_j^2, \sigma_{i,j}^2 (y_j + y_k)^2 + \sigma_{i,0}^2 y_k^2 + \sigma_{i,k}^2 y_j^2\} \quad (24b)$$

It can be observed that the denominator of (24a) and (24b) is proportional to the magnitude of the area of the triangle formed using the three nodes. Thus, it is desired to maximize the area of the triangle in a bounded region. On the other hand, their numerators depend on the magnitude of the x and y coordinates of the receivers. For a lesser magnitude of the x and y coordinates, the area of the triangle decreases. Thus, the area under the triangle needs to be optimized to minimize the trace and maximum eigenvalue.  $\square$

One of the sub-optimal solution for the Lemma 1 can be obtained using the following corollary.

**Corollary 1.** *For the given variances,  $\{\sigma_{i,q}^2\}$ ;  $q \in \{0, j, k\}$ , if the receivers are placed at orthogonal axis in Lemma 1, then,  $\text{tr}(\text{cov}(\hat{\alpha}_i, \hat{\beta}_i))$  or  $\kappa_{\max}(\text{cov}(\hat{\alpha}_i, \hat{\beta}_i))$  can be minimized by maximizing the area of the triangle formed using the three nodes in a given bounded region.*

*Proof.* If the receivers  $\mathcal{R}_j$  and  $\mathcal{R}_k$  are placed at the x and y axes (orthogonal axes) of the Cartesian coordinates in Lemma 1, then their coordinates are given by:  $(x_j, 0)$  and  $(0, y_k)$ , respectively. After, substituting these coordinates in

(24a) and (24b), we get:

$$\text{tr}(\text{cov}(\hat{\alpha}_i, \hat{\beta}_i)) = \frac{\sigma_{i,j}^2 + \sigma_{i,k}^2}{y_k^2} + \frac{\sigma_{i,j}^2 + \sigma_{i,0}^2}{x_j^2}, \quad (25a)$$

$$\kappa_{\max}(\text{cov}(\hat{\alpha}_i, \hat{\beta}_i)) = \max \left\{ \frac{\sigma_{i,j}^2 + \sigma_{i,0}^2}{x_j^2}, \frac{\sigma_{i,j}^2 + \sigma_{i,k}^2}{y_k^2} \right\}. \quad (25b)$$

From (25a) and (25b), it is evident that  $\text{tr}(\text{cov}(\hat{\alpha}_i, \hat{\beta}_i))$  and  $\kappa_{\max}(\text{cov}(\hat{\alpha}_i, \hat{\beta}_i))$  can be minimized by maximizing the magnitude of  $x_j$  and  $y_k$  which is equivalent to maximizing the magnitude of the area of right angled triangle formed using the three nodes.  $\square$

From the above, we can now determine the trace and the eigenvalue of  $\text{cov}(\hat{\alpha}_i, \hat{\beta}_i)$  using Lemma 2 below via the location of the target is estimated using the average location in (18a) or the nearest-neighbor-based selection in (21) when  $Z$  receivers are deployed along with the AN in a given region.

**Lemma 2.** For the given variances,  $\sigma_{i,0,t}^2$ ,  $\sigma_{i,1,t}^2$ , and  $\sigma_{i,2,t}^2$ ;  $t \in \{1, \dots, \mathfrak{N}\}$  of the square of the estimated distances from the nodes,  $\mathcal{A}_0$ ,  $\mathcal{R}_{i,1,t}$ , and  $\mathcal{R}_{i,2,t}$  in the  $t$ th triangulation and the coordinates of the AN and receivers at  $(0, 0)$  and  $(x_{1,t}, y_{1,t})$ ,  $((x_{2,t}, y_{2,t})$ ,  $\text{tr}(\text{cov}(\hat{\alpha}_i, \hat{\beta}_i))$  and  $\kappa_{\max}(\text{cov}(\hat{\alpha}_i, \hat{\beta}_i))$  of the estimated location  $(\hat{\alpha}_i, \hat{\beta}_i)$  by averaging all the independent estimated locations in  $\mathfrak{N}$  triangulations is given by:

$$\text{tr}(\text{cov}(\hat{\alpha}_i, \hat{\beta}_i)) = \frac{1}{\mathfrak{N}^2} \sum_{t=1}^{\mathfrak{N}} [\sigma_{i,1,t}^2 \{(x_{1,t} + x_{2,t})^2 + (y_{1,t} + y_{2,t})^2\} + \sigma_{i,0,t}^2 (x_{2,t}^2 + y_{2,t}^2) + \sigma_{i,k,t}^2 (x_{1,t}^2 + y_{1,t}^2)] / (x_{1,t}y_{2,t} - x_{2,t}y_{1,t})^2, \quad (26a)$$

$$\kappa_{\max}(\text{cov}(\hat{\alpha}_i, \hat{\beta}_i)) = \frac{1}{\mathfrak{N}^2} \max \left\{ \sum_{t=1}^{\mathfrak{N}} [\sigma_{i,1,t}^2 (x_{1,t} + x_{2,t})^2 + \sigma_{i,0,t}^2 x_{2,t}^2 + \sigma_{i,2,t}^2 x_{1,t}^2] / \mathcal{D}_t^2, \sum_{t=1}^{\mathfrak{N}} [\sigma_{i,1,t}^2 (y_{1,t} + y_{2,t})^2 + \sigma_{i,0,t}^2 y_{2,t}^2 + \sigma_{i,2,t}^2 y_{1,t}^2] / \mathcal{D}_t^2 \right\}, \quad (26b)$$

where  $\mathcal{D}_t = (x_{1,t}y_{2,t} - x_{2,t}y_{1,t})$ , whereas  $\mathfrak{N} = \mathcal{Z}$  and  $= |\mathcal{S}_{n^*}| + 1$  for the averaged approaches in (18a) and (21), respectively. The  $\text{tr}(\text{cov}(\hat{\alpha}_i, \hat{\beta}_i))$  and  $\kappa_{\max}(\text{cov}(\hat{\alpha}_i, \hat{\beta}_i))$  can be minimized by optimizing the magnitude of the area of each triangulation.

*Proof.* The proof of Lemma 2 can be followed similarly to Lemma 1.  $\square$

Next, using Lemma 2, we show that the sub-optimal solution for Lemma 2 is to place the two receivers with multiple uncorrelated antennas at the orthogonal axis with maximum underlying area.

**Lemma 3.** For the given variances of the square estimation of the distances from the AN and the  $\mathcal{Z}$  receivers, if the receivers are split equally into two groups and they are placed on orthogonal axes, then, the sub-optimal solution to minimize  $\text{tr}(\text{cov}(\hat{\alpha}_i, \hat{\beta}_i))$  and  $\kappa_{\max}(\text{cov}(\hat{\alpha}_i, \hat{\beta}_i))$  is equivalent to the obtained trace and maximum eigenvalue of the covariance

of the estimated target location in the topology where two receivers, each with  $Z/2$  uncorrelated antennas, are placed on the orthogonal axes such that magnitude of the underlying area is maximum in the given bounded region.

*Proof.* If the two groups of  $Z/2$  receivers are placed at the orthogonal axes, using the Corollary 1 of Lemma 1, the trace and maximum eigenvalue of the covariance can be expressed as:

$$\text{tr}(\text{cov}(\hat{\alpha}_i, \hat{\beta}_i)) = \frac{4}{Z^2} \sum_{t=1}^{Z^2/4} \left[ \frac{\sigma_{i,1,t}^2 + \sigma_{i,0,t}^2}{x_{1,t}^2} + \frac{\sigma_{i,1,t}^2 + \sigma_{i,2,t}^2}{y_{2,t}^2} \right] \quad (27a)$$

$$\kappa_{\max}(\text{cov}(\hat{\alpha}_i, \hat{\beta}_i)) = \frac{4}{Z^2} \max \left\{ \sum_{t=1}^{Z^2/4} \frac{\sigma_{i,1,t}^2 + \sigma_{i,0,t}^2}{x_{1,t}^2}, \sum_{t=1}^{Z^2/4} \frac{\sigma_{i,1,t}^2 + \sigma_{i,2,t}^2}{y_{2,t}^2} \right\} \quad (27b)$$

From (27a) and (27b), it is evident that in a given bounded region, the two groups of receivers should be placed on the orthogonal axes such that the magnitude of the area of the underlying triangles should be maximum. Thus, the receivers of the two groups lie at two points spanned to their maximum length on their respective orthogonal axes under the given bounded region. This is equivalent to three nodes deployed in the region where each of the two receivers has  $Z/2$  uncorrelated antennas.  $\square$

Now, we describe the amount of the reduction in the trace and the maximum eigenvalue of the covariance matrix in the following lemma, when the three nodes consist of multiple antennas.

**Lemma 4.** If each of the three nodes, the AN  $\mathcal{A}_0$  and the receivers  $\mathcal{R}_1$  and  $\mathcal{R}_2$ , has  $\mathcal{N}$  number of independent antennas (the separation between the two antennas at a node is greater than  $\lambda/2$ ) and  $\mathcal{R}_1$  and  $\mathcal{R}_2$  are placed at orthogonal axes, then, the average trace  $\text{tr}(\text{cov}(\hat{\alpha}_{i,\text{avg}}, \hat{\beta}_{i,\text{avg}}))$  and the maximum eigenvalue  $\kappa_{\max}(\text{cov}(\hat{\alpha}_{i,\text{avg}}, \hat{\beta}_{i,\text{avg}}))$ , obtained using the approach in (18a), are reduced by a factor  $\mathcal{N}^3$  compared to the obtained values of the counterparts in (25) of Corollary 1. Here, we assume that the variances  $\sigma_{i,0,t}^2$ ,  $\sigma_{i,1,t}^2$ , and  $\sigma_{i,2,t}^2$  remain same for all  $t \in \{1, \dots, \mathfrak{N}\}$ , where  $\mathfrak{N} = \mathcal{N}^3$ .

*Proof.* As each of the three nodes has  $\mathcal{N}$  independent antennas, the total combination of independent geometrical triangulations formed is  $\mathfrak{N} = \mathcal{N}^3$ . Thus, the total number of samples of each of the estimated range squares  $\rho_{i,0}^2$ ,  $\rho_{i,1}^2$ , and  $\rho_{i,2}^2$  of the  $i$ th target from the respective nodes  $\mathcal{A}_0$ ,  $\mathcal{R}_1$ , and  $\mathcal{R}_2$  is  $\mathcal{N}^3$ . For the estimated average target location using (18a), where  $\mathcal{Z} = \mathcal{N}^3$ . Therefore, from the central limit theorem, the random variables  $\rho_{i,0}^2$ ,  $\rho_{i,1}^2$ , and  $\rho_{i,2}^2$  follow the Gaussian distribution with variances  $\rho_{i,0}^2/\mathcal{N}^3$ ,  $\rho_{i,1}^2/\mathcal{N}^3$ , and  $\rho_{i,2}^2/\mathcal{N}^3$ . The trace and the maximum eigenvalue can be expressed as:  $\text{tr}(\text{cov}(\hat{\alpha}_{i,\text{avg}}, \hat{\beta}_{i,\text{avg}})) = \text{tr}(\text{cov}(\hat{\alpha}_i, \hat{\beta}_i))/\mathcal{N}^3$  and  $\kappa_{\max}(\text{cov}(\hat{\alpha}_{i,\text{avg}}, \hat{\beta}_{i,\text{avg}})) = \kappa_{\max}(\text{cov}(\hat{\alpha}_i, \hat{\beta}_i))/\mathcal{N}^3$ , where  $\text{tr}(\text{cov}(\hat{\alpha}_i, \hat{\beta}_i))$  and  $\kappa_{\max}(\text{cov}(\hat{\alpha}_i, \hat{\beta}_i))$  are given by (25).  $\square$

#### IV. SENSING IMPROVEMENT USING CRW-BASED KF

In this section, we describe the trajectory estimation of moving targets using correlated random walk (CRW) based Kalman filtering (KF). Typically, the movements of the targets like humans, animals, vehicles, and uncrewed aerial vehicles (UAVs) are not entirely random, but they follow the same direction for a while.

##### A. CRW-Based Prediction Model

CRW exploits the Ornstein-Uhlenbeck (OU) process to provide the prediction model [21]. Using it, the velocity  $\mathbf{v}_{i,t} = [v_{i,\alpha,t}, v_{i,\beta,t}]^T$  (with its  $x$  and  $y$  components  $v_{i,\alpha,t}$  and  $v_{i,\beta,t}$ ) of the  $i$ th target at time  $t$  is modeled as:

$$d\mathbf{v}_{i,t} = \delta_i(\mathbf{v}_{i,t} - \boldsymbol{\omega}_i)dt + \psi_i d\mathbf{W}_{i,t}, \quad (28)$$

where  $\delta_i$  is the velocity autocorrelation coefficient,  $\boldsymbol{\omega}_i$  is the mean velocity,  $\psi_i$  is the diffusion parameter and  $W_{i,t}$  is the Wiener random process. After solving (28) in continuous time, we get  $\mathbf{v}_{i,t}$  in (29a), which is further represented in the discrete time domain as in (29b).

$$\mathbf{v}_{i,t} = \boldsymbol{\omega}_i + (\mathbf{v}_{i,0} - \boldsymbol{\omega}_i)e^{-\delta_i t} + \psi_i \int_0^t e^{-\delta_i(t-s)} d\mathbf{W}_{i,s}, \quad (29a)$$

$$\mathbf{v}_{i,t+1} = \mathbf{v}_{i,t}e^{-\delta_i \Delta t} + \mathbf{n}_{i,t}^v \quad (29b)$$

where  $\mathbf{v}_{i,0} = [v_{i,\alpha,0}, v_{i,\beta,0}]^T$  is the initial velocity of the target and  $\mathbf{n}_{i,t}^v = [n_{i,t}^{v\alpha}, n_{i,t}^{v\beta}]^T$  is the Gaussian noise added to the velocity update. Using (29a), the location  $\mathbf{l}_{i,t} = [\alpha_{i,t}, \beta_{i,t}]$  of the target is updated as in (30a). Using it, the location update in discrete time, i.e., the location at  $t + 1$ th time is updated from the location at  $t$ th time via (30b).

$$\mathbf{l}_{i,t} = \mathbf{l}_{i,0} + \int_0^t \mathbf{v}_{i,s} ds \quad (30a)$$

$$\mathbf{l}_{i,t+1} = \mathbf{l}_{i,t} + \frac{1 - e^{-\delta_i \Delta t}}{\delta_i} \mathbf{v}_{i,t} + \mathbf{n}_{i,t}^l, \quad (30b)$$

where  $\mathbf{n}_{i,t}^l = [n_{i,t}^{\alpha}, n_{i,t}^{\beta}]^T$  is the Gaussian noise added to the location update. Next, we use the prediction model based on CRW in the KF algorithm to further enhance the accuracy in sensing of the targets. In this regard, first, we define the state  $\mathbf{S}_t$  at time  $t$  of the  $i$ th target as:  $\mathbf{S}_t \triangleq [\alpha_{i,t}, \beta_{i,t}, v_{i,x,t}, v_{i,y,t}]^T$ . Further, using (29b) and (30b), the state transition is given in (31a) and corresponding transition matrix  $\mathbf{T}_i$  is expressed in (31b) which is obtained by the Jacobian  $J_f(\mathbf{s}_{i,t})$  of the state transition [22].

$$\mathbf{s}_{i,t+1} = \mathbf{T}_i \mathbf{s}_{i,t} + \mathbf{n}_{i,t}^s, \quad (31a)$$

$$\mathbf{T}_i = \begin{bmatrix} 1 & 0 & \frac{1 - e^{-\delta_i \Delta t}}{\delta_i} & 0 \\ 0 & 1 & 0 & \frac{1 - e^{-\delta_i \Delta t}}{\delta_i} \\ 0 & 0 & e^{-\delta_i \Delta t} & 0 \\ 0 & 0 & 0 & e^{-\delta_i \Delta t} \end{bmatrix} \quad (31b)$$

where  $\mathbf{n}_{i,t}^s = [n_{i,t}^{\alpha}, n_{i,t}^{\beta}, n_{i,t}^{v\alpha}, n_{i,t}^{v\beta}]^T$  is the noise process. Noise  $\mathbf{n}_{i,t}^s$  captures the uncertainties in the prediction model with the covariance matrix  $\mathbf{Q}_{i,t} = \mathbb{E}[\mathbf{n}_{i,t}^s \mathbf{n}_{i,t}^{sT}]$  with  $\mathbb{E}[\mathbf{n}_{i,t}^s \mathbf{n}_{i,t'}^{sT}] = 0$  for  $t \neq t'$ .

---

**Algorithm 1** KF function  $f_{KF}$  to estimate the state  $\mathbf{s}_{i,t}^a$ .

---

- 1: System parameters  $\mathbf{T}_i$  and  $\mathbf{V}_i$
  - 2: **Input:**  $\mathbf{Q}_{i,t-1}$ ,  $\mathbf{R}_{i,t}$ ,  $\mathbf{s}_{i,t-1}^a$ ,  $\mathbf{P}_{i,t-1}$ , and the measurement  $\mathbf{z}_{i,t}$
  - 3: Determine the forecasted state:  $\mathbf{s}_{i,t}^f = \mathbf{T}_i \mathbf{s}_{i,t-1}^a$
  - 4: Update the forecast error covariance:  $\mathbf{P}_{i,t}^f = \mathbf{T}_i \mathbf{P}_{i,t-1} \mathbf{T}_i^T + \mathbf{Q}_{i,t-1}$
  - 5: Determine Kalman gain:  $\mathbf{K}_{i,t} = \mathbf{P}_{i,t}^f \mathbf{V}_i^T (\mathbf{V}_i \mathbf{P}_{i,t}^f \mathbf{V}_i^T + \mathbf{R}_{i,t})^{-1}$
  - 6: Update state estimate:  $\mathbf{s}_{i,t}^a = \mathbf{s}_{i,t}^f + \mathbf{K}_{i,t} (\mathbf{z}_{i,t} - \mathbf{V}_i \mathbf{s}_{i,t}^f)$
  - 7: Update posterior error covariance:  $\mathbf{P}_{i,t} = (\mathbf{I} - \mathbf{K}_{i,t} \mathbf{V}_i) \mathbf{P}_{i,t}^f (\mathbf{I} - \mathbf{K}_{i,t} \mathbf{V}_i)^T + \mathbf{K}_{i,t} \mathbf{R}_{i,t} \mathbf{K}_{i,t}^T$
  - 8: **Output:** State estimate  $\mathbf{s}_{i,t}^a$  and the error covariance  $\mathbf{P}_{i,t}$
- 

##### B. Measurement Model and Trajectory Estimation Using KF

As described in Section III, the measurement  $\mathbf{z}_{i,t}$  for the location and velocity of the  $i$ th target is obtained from the average or selection based approaches using (18) or (21). The measurement  $\mathbf{z}_{i,t}$  is related to the state  $\mathbf{s}_{i,t}$  in the prediction model, which is expressed as:

$$\mathbf{z}_{i,t} = \mathbf{V}_i \mathbf{s}_{i,t} + \mathbf{n}_{i,t}^z, \quad (32)$$

where  $\mathbf{V}_i$  is the observation matrix and  $\mathbf{n}_{i,t}^z$  is the zero-mean Gaussian noise with covariance matrix  $\mathbf{R}_i = \mathbb{E}[\mathbf{n}_{i,t}^z \mathbf{n}_{i,t}^{zT}]$  and  $\mathbb{E}[\mathbf{n}_{i,t}^z \mathbf{n}_{i,t'}^{zT}] = 0$ . As in the measurement, we consider all the four  $x$  and  $y$  components of the location and velocity of the target, therefore,  $\mathbf{V}_i = \mathbf{I}_4$ , where  $\mathbf{I}_n$  is an identity matrix of size  $n \times n$ .

Using (31a) and (32), the KF performs the forecast using the prediction and data correction under the noisy measurement to enhance the accuracy in the estimation. The KF algorithm starts with the initialization of  $\mathbf{T}_i$ ,  $\mathbf{V}_i$ , prediction error covariance matrix  $\mathbf{Q}_{i,0}$ , measurement  $\mathbf{z}_{i,1}$  with noise covariance matrix  $\mathbf{R}_{i,1}$  and an estimate of the initial state  $\mathbf{s}_{i,0}^a = \mathbb{E}[\mathbf{s}_{i,0}]$  with error covariance matrix  $\mathbf{P}_{i,0} = \mathbb{E}[(\mathbf{s}_{i,0} - \mathbf{s}_{i,0}^a)(\mathbf{s}_{i,0} - \mathbf{s}_{i,0}^a)^T]$ , where  $\mathbf{s}_{i,0} = [\alpha_{i,0}, \beta_{i,0}, v_{i,\alpha,0}, v_{i,\beta,0}]^T$ . Thereafter, as described in Algorithm 1, for the  $t$ th time step,  $\mathbf{Q}_{i,t-1}$ ,  $\mathbf{R}_{i,t}$ ,  $\mathbf{s}_{i,t-1}^a$ ,  $\mathbf{P}_{i,t-1}$ , and  $\mathbf{z}_{i,t}$  are inputted to the function  $f_{KF}$  that determines  $\mathbf{s}_{i,t}^f$ ,  $\mathbf{P}_{i,t}^f$ ,  $\mathbf{K}_{i,t}$ ,  $\mathbf{s}_{i,t}^a$ , and  $\mathbf{P}_{i,t}$ . Finally, the function provides the estimate of the state  $\mathbf{s}_{i,t}^a$  and the covariance  $\mathbf{P}_{i,t}$ .

*Complexity:* The computational cost of one KF update in Algorithm 1 depends on the dimensions  $n$  and  $m$  of the state  $\mathbf{s}_t$  and measurement  $\mathbf{z}_t$  vectors. In the prediction step, the forecasted state  $\mathbf{s}_{i,t}^f$  is computed in Step 3 requires  $O(n^2)$  operations. While the forecast covariance  $\mathbf{P}_{i,t}^f$  in Step 4 involves two matrix multiplications which costs  $O(n^3)$ . In Step 5, the Kalman gain  $\mathbf{K}_{i,t}$  is computed in  $O(n^2 m + nm^2)$  operations, and the state update  $\mathbf{s}_{i,t}^a$  costs  $O(nm)$  in Step 6. Further, update of the covariance matrix  $\mathbf{P}_{i,t}$  takes  $O(n^3 + n^2 m + nm^2)$  operations in Step 7. Thus, the overall update complexity is  $O(n^3 + n^2 m + nm^2)$ . Further, for  $m \leq n$ , the complexity is reduced to  $O(n^3)$ . Next, we describe the iterative algorithms that incorporate the KF in both active sensing and joint passive sensing and communication to enhance their performance.

In Algorithm 2, the active sensing as described in Sec-

**Algorithm 2** Improved active sensing using KF.

---

```

1: System parameters:  $\{\mathbf{T}_i\}$ ,  $\{\mathbf{V}_i\}$  for  $i \in \{1, \dots, P\}$ , and
   others independent parameters
2: Input:  $\{\mathbf{s}_{i,0}^a\}$ ,  $\{\mathbf{P}_{i,0}\}$ 
3: for each  $t \in \{1, \dots, \mathcal{T}\}$  do
4:   for each  $i \in \{1, \dots, P\}$  do
5:     for each  $j \in \{0, \dots, Z\}$  do
6:       Determine  $(\widehat{\tau}_{i,j,t}, \widehat{\nu}_{i,j,t})$  and  $\widehat{h}_{i,j,t}$  from (9)
       using the known data  $\mathbf{d}$ 
7:       Determine the range  $\widehat{\rho}_{i,j,t}$  and the radial velocity
        $\widehat{v}_{i,j,t}$  from (10)
8:     end for
9:     Get  $\mathbf{Q}_{i,t-1}$  and determine the averaged or se-
     lection based estimated observation vector  $\mathbf{z}_{i,t} =$ 
      $[\widehat{\alpha}_{i,t}, \widehat{\beta}_{i,t}, \widehat{v}_{i,x,t}, \widehat{v}_{i,y,t}]^T$  using (18) or (21) and get the
     noise covariance  $\mathbf{R}_{i,t}$ 
10:    Determine  $\mathbf{s}_{i,t}^a$  and  $\mathbf{P}_{i,t}$  using the function
      $f_{KF}(\mathbf{s}_{i,t-1}^a, \mathbf{P}_{i,t-1}, \mathbf{Q}(i, t-1), \mathbf{R}_{i,t})$  in Algorithm 1
11:    end for
12: end for

```

---

tion II-D is further improved using the KF. Here, for each target  $i$  and receiver  $j$  at a given time  $t$ , the delay  $\widehat{\tau}_{i,j}$ , Doppler  $\widehat{\nu}_{i,j}$ , and the channel gain  $\widehat{h}_{i,j}$  are estimated, followed by the range  $\widehat{\rho}_{i,j}$  and the radial velocity  $\widehat{v}_{i,j}$ . Then, for each target  $i$ , the measurement vector  $\mathbf{z}_{i,t}$  is determined; thereafter, using KF function  $f_{KF}$  in Algorithm 1, the sensing variables are estimated.

*Complexity:* The computational cost of Algorithm 2 depends on the number of time steps  $\mathcal{T}$ , the number of targets  $P$ , the number of receivers  $Z$ , and the state dimension  $n$ . For each target  $i$  and receiver  $j$  at each time instant  $t$ , the estimation of  $(\widehat{\tau}_{i,j,t}, \widehat{\nu}_{i,j,t})$  and  $\widehat{h}_{i,j,t}$  in Step 6 involves the two-dimensional delay–Doppler correlation search, which requires  $\mathcal{O}(G_\tau G_\nu MN)$  operations per path. The subsequent computation of range  $\widehat{\rho}_{i,j,t}$  and radial velocity  $\widehat{v}_{i,j,t}$  in Step 7 involves only scalar operations with negligible cost. Thus, for all  $Z+1$  receivers, Steps 6 and 7 contribute  $\mathcal{O}((Z+1)G_\tau G_\nu MN)$  per target per time step. Forming the measurement vector  $\mathbf{z}_{i,t}$  in Step 9 requires  $\mathcal{O}(Z)$ , which is negligible compared to the correlation search. In Step 10, the Kalman filter update in Algorithm 1 has complexity  $\mathcal{O}(n^3 + n^2m + nm^2)$ , which reduces to  $\mathcal{O}(n^3)$  for  $m \leq n$ . Hence, the overall complexity of Algorithm 2 is  $\mathcal{O}(\mathcal{T} \cdot P \cdot ((Z+1)G_\tau G_\nu MN + n^3))$ . This shows that the algorithm grows linearly with the number of time steps, targets, and receivers, but quadratically with the delay–Doppler grid resolution, while also depending cubically on the state dimension through the Kalman filter update.

**Algorithm 3.** Improved passive sensing and communication using KF.

---

```

1: System parameters:  $\{\mathbf{T}_i\}$  and  $\{\mathbf{V}_i\}$  for  $i \in \{1, \dots, P\}$ ,
   thresholds  $\epsilon_d, \epsilon_h, \epsilon_\tau, \epsilon_\nu$ , and other independent parameters
2: Input:  $\{\mathbf{s}_{i,0}^a\}$ ,  $\{\mathbf{P}_{i,0}\}$ 
3: for each  $t \in \{1, \dots, \mathcal{T}\}$  do
4:   for each  $i \in \{1, \dots, P\}$  do
5:     for each  $j \in \{0, \dots, Z\}$  do

```

---

```

6:     Initially, estimate  $(\widehat{h}_{i,j,t}^{(0)}, \widehat{\tau}_{i,j,t}^{(0)}, \widehat{\nu}_{i,j,t}^{(0)})$  via the
     coarse estimation using the pilot  $\mathbf{d}_P$  in (11)
7:     Determine  $\widehat{\rho}_{i,j,t}^{(0)}$  and  $\widehat{v}_{i,j,t}^{(0)}$  using (10)
8:   end for
9:   Determine the average or selection based estimated
     location  $(\widehat{\alpha}_{i,t}^{(0)}, \widehat{\beta}_{i,t}^{(0)})$  and velocity  $(\widehat{v}_{i,x,t}^{(0)}, \widehat{v}_{i,y,t}^{(0)})$  using (18)
     or (21)
10:  for each  $j \in \{0, \dots, Z\}$  do
11:    Using the reverse process of (10), find the delay
      $\overline{\tau}_{i,j,t}^{(0)}$  and the Doppler shift  $\overline{\nu}_{i,j,t}^{(0)}$ 
12:    Using  $(\overline{\tau}_{i,j,t}^{(0)}, \overline{\nu}_{i,j,t}^{(0)})$ , obtain  $\overline{h}_{i,j,t}^{(0)}$  for pilot  $\mathbf{d}_P$ 
     from (9b)
13:  end for
14:  end for
15:  Initialize outer loop:  $\text{iter}_{out} = 0$ ,  $\text{conv}_{out} =$ 
     ‘FALSE’,  $(\mathbf{h}_j^{curr}, \boldsymbol{\tau}_j^{curr}, \boldsymbol{\nu}_j^{curr}) = (\widehat{\mathbf{h}}_j^{(0)}, \widehat{\boldsymbol{\tau}}_j^{(0)}, \widehat{\boldsymbol{\nu}}_j^{(0)})$ , and
     flags  $(f_1, \dots, f_P) = (\text{‘FALSE’}, \dots, \text{‘FALSE’})$ 
16:  while NOT convout do
17:    for each  $j \in \{0, \dots, Z\}$  do
18:       $\text{iter}_{out} = \text{iter}_{out} + 1$ 
19:      Data Estimation (inner loop):
20:      Initialize  $\mathbf{d}_{j,t}^{(0)} = \mathbf{0}$ ,  $q = 0$ , and  $\text{conv}_{in} =$ 
     ‘FALSE’
21:      while NOT convin do
22:        Compute  $\nabla J(\mathbf{d}_{j,t}^{(q)})$  using (14a)
23:        Compute  $\mathbf{d}_{j,t}^{(q+1)}$  using (14b)
24:        if  $\|\mathbf{d}_{j,t}^{(q+1)} - \mathbf{d}_{j,t}^{(q)}\| < \epsilon_d$  then
25:           $\text{conv}_{in} = \text{‘True’}$ 
26:        else
27:           $q = q + 1$ 
28:        end if
29:      end while
30:      Perform  $\mathbf{d}'_{j,t} = \mathbf{d}_{j,t}^{(q+1)}$  and  $\mathbf{D}'_{j,t} = \text{vec}^{-1}(\mathbf{d}'_{j,t})$ 
31:      Obtain information data  $\mathbf{D}'_{I,j,t} = \mathbf{D}'_{j,t} - \mathbf{D}_P$ 
32:      Obtain  $\widehat{\mathbf{D}}_{I,j,t}$  from  $\mathbf{D}'_{j,t}$  using sybmol-wise
     demodulation from (15)
33:      Refined channel estimation (active sensing):
34:      Perform  $\widehat{\mathbf{D}}_{j,t} = \widehat{\mathbf{D}}_{I,j,t} + \mathbf{D}_P$  and  $\widehat{\mathbf{d}}_{j,t} =$ 
      $\text{vec}(\widehat{\mathbf{D}}_{j,t})$ 
35:      if  $f_j == \text{‘FALSE’}$  then
36:        Obtain  $(\widehat{\mathbf{h}}_{j,t}, \widehat{\boldsymbol{\tau}}_{j,t}, \widehat{\boldsymbol{\nu}}_{j,t})$  from (11) using the
     data  $\widehat{\mathbf{d}}_{j,t}$ 
37:        Determine the range  $\widehat{\rho}_{j,t}$  and the radial
     velocity  $\widehat{v}_{j,t}$  using (10)
38:      end if
39:    end for
40:    for each  $i \in \{1, \dots, P\}$  do
41:      Get  $\mathbf{Q}_{i,t-1}$  and determine the averaged or
     selection based estimated observation vector  $\mathbf{z}_{i,t} =$ 
      $[\widehat{\alpha}_{i,t}, \widehat{\beta}_{i,t}, \widehat{v}_{i,x,t}, \widehat{v}_{i,y,t}]^T$  using (18) or (21) and get the
     noise covariance  $\mathbf{R}_{i,t}$ 
42:      Determine  $\mathbf{s}_{i,t}^a$  and  $\mathbf{P}_{i,t}$  using the function
      $f_{KF}(\mathbf{s}_{i,t-1}^a, \mathbf{P}_{i,t-1}, \mathbf{Q}(i, t-1), \mathbf{R}_{i,t})$  in Algorithm 1
43:    end for
44:    for each  $j \in \{0, \dots, Z\}$  do
45:      if  $f_j == \text{‘FALSE’}$  then

```

```

46:         Using the reverse process of (10), find the
delay  $\tau_{j,t}^{new}$  and the Doppler shift  $\nu_{j,t}^{new}$ 
47:         Using  $(\tau_{j,t}^{new}, \nu_{j,t}^{new})$ , obtain  $\mathbf{h}_{j,t}^{new}$  for data
 $\hat{\mathbf{d}}_{j,t}$  from (9b)
48:         if  $\|\mathbf{h}_{j,t}^{new} - \mathbf{h}_{j,t}^{curr}\| < \epsilon_h$  &  $\|\tau_{j,t}^{new} - \tau_{j,t}^{curr}\| < \epsilon_\tau$  &  $\|\nu_{j,t}^{new} - \nu_{j,t}^{curr}\| < \epsilon_\nu$  then
49:              $f_j = \text{'TRUE'}$ 
50:         else
51:              $(\mathbf{h}_{j,t}^{curr}, \tau_{j,t}^{curr}, \nu_{j,t}^{curr}) = (\mathbf{h}_{j,t}^{new}, \tau_{j,t}^{new}, \nu_{j,t}^{new})$ 
52:         end if
53:     end if
54: end for
55: if  $(f_1, \dots, f_P) = (\text{'TRUE'}, \dots, \text{'TRUE'})$  then
56:      $\text{conv}_{out} = \text{'TRUE'}$ 
57: end if
58: end while
59: end for

```

In Algorithm 3, for each time  $t$ , target  $i$  and receiver  $j$ , the coarse estimates of the delay, Doppler, and channel gain,  $(\hat{h}_{i,j,t}^{(0)}, \hat{\tau}_{i,j,t}^{(0)}, \hat{\nu}_{i,j,t}^{(0)})$ , are first obtained using the pilot  $\mathbf{d}_P$ . These estimates are mapped to the range and velocity domain, from which the coarse location and velocity of each target are determined via the averaging or selection methods in (18) and (21). The reverse mapping from range and velocity is then applied to reconstruct channel parameters that serve as initialization for iterative refinement. The refinement is carried out in an *outer loop* that alternates between communication data detection and sensing parameter update. Within the inner loop, the received data is iteratively refined using a gradient-based update (cf. (14a), (14b)) until convergence within the tolerance  $\epsilon_d$ . The recovered symbols are demodulated to obtain the information data, which are then used to improve the channel estimates  $(\hat{\mathbf{h}}_{j,t}, \hat{\tau}_{j,t}, \hat{\nu}_{j,t})$ . For each target  $i$ , the refined measurements are aggregated into the observation vector  $\mathbf{z}_{i,t} = [\hat{\alpha}_{i,t}, \hat{\beta}_{i,t}, \hat{v}_{i,x,t}, \hat{v}_{i,y,t}]^T$ . The KF function  $f_{KF}$  from Algorithm 1 is then applied to update the state  $\mathbf{s}_{i,t}^a$  and error covariance  $\mathbf{P}_{i,t}$ . This ensures reliable tracking of the location and velocity despite noise and estimation errors.

The outer loop continues until the differences between successive channel estimates fall below the predefined thresholds  $(\epsilon_h, \epsilon_\tau, \epsilon_\nu)$ . Once satisfied for all receivers, convergence is declared and the algorithm terminates. In this way, Algorithm 3 integrates communication data recovery and passive sensing in a closed-loop process, where improved data detection enhances channel estimation and, in turn, refined channel estimates improve sensing and tracking performance through the KF.

*Complexity:* The computational cost of Algorithm 3 depends on the number of time steps  $\mathcal{T}$ , the number of targets  $P$ , the number of receivers  $Z$ , the state dimension  $n$ , and the average number of inner and outer iterations, denoted by  $I_{in}$  and  $I_{out}$ , respectively. For each time instant  $t$ , target  $i$ , and receiver  $j$ , the coarse estimation of  $(\hat{h}_{i,j,t}^{(0)}, \hat{\tau}_{i,j,t}^{(0)}, \hat{\nu}_{i,j,t}^{(0)})$  in Step 6 requires a delay-Doppler correlation search using the pilot  $\mathbf{d}_P$ , which incurs  $\mathcal{O}(G_\tau G_\nu MN)$  operations. Mapping these coarse estimates to range and velocity in Step 7 and the reverse mapping in Steps 9-13 involve only scalar

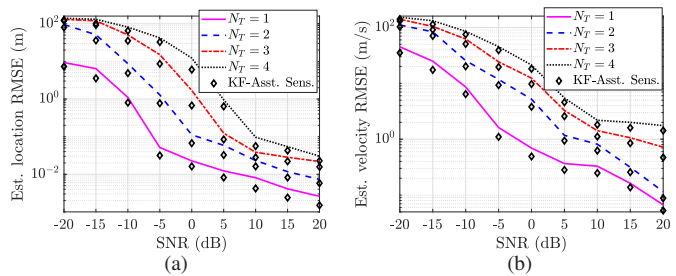


Fig. 3. RMSE improvement with SNR for different numbers of targets.

computations with negligible cost compared to the correlation search. Thus, the initial coarse estimation across all receivers contributes  $\mathcal{O}((Z+1)G_\tau G_\nu MN)$  per target per time instant. Within the outer loop, communication data detection is refined through an inner loop of gradient-based updates in Steps 22-27. Each gradient evaluation and update requires  $\mathcal{O}(MN)$  operations, and with  $I_{in}$  iterations, the total cost per receiver per outer iteration is  $\mathcal{O}(I_{in}MN)$ . Demodulation and symbol decisions in Step 32 require  $\mathcal{O}(MN)$ , which is absorbed into this term. Refined channel estimation using recovered data in Step 36 again involves a delay-Doppler correlation search of cost  $\mathcal{O}(G_\tau G_\nu MN)$ . However, this step is performed conditionally depending on the convergence flag, and repeated over  $I_{out}$  outer iterations until convergence. For each target  $i$ , forming the observation vector  $\mathbf{z}_{i,t}$  and updating the state and covariance via the KF function  $f_{KF}$  in Steps 41-42 require  $\mathcal{O}(n^3)$ , as in Algorithm 2. Finally, the convergence checks for thresholds  $(\epsilon_h, \epsilon_\tau, \epsilon_\nu)$  in Step 48 involve vector norm evaluations of cost  $\mathcal{O}(Z)$ , negligible relative to correlation searches and matrix operations. Combining these contributions, the overall complexity of Algorithm 3 is  $\mathcal{O}(\mathcal{T} \cdot P \cdot ((Z+1)(G_\tau G_\nu MN + I_{out}(I_{in}MN + G_\tau G_\nu MN)) + n^3))$ .

## V. NUMERICAL RESULTS AND CONCLUSION

In this section, we evaluate the performance of the proposed analysis using the obtained numerical results. From Lemma 3, we find that the topology which consists of three nodes with multiple independent antennas, covering the maximum triangular area in a bounded region, is more efficient in sensing than the multiple nodes of a single antenna, distributed randomly over the region. Therefore, unless specified, we consider the former topology for the ISAC performance. The other default values of the system parameters are listed in the Table I. Further, the trajectories for the moving targets are generated using Algorithm A.1<sup>2</sup> in Appendix A to evaluate the performance of KF-assisted ISAC.

Using Figs. 3 and 4, we compare the performance of active sensing and KF-assisted active sensing in reduction of the root-mean-square error (RMSE) for the estimated location and velocity of the targets. We observe that the KF-assisted active sensing always performs better for any number of targets, because, the former balances the noises due to prediction and measurement and avoids the overfitting towards any of

<sup>2</sup>The values of the used parameters in Algorithm A.1 are given in the algorithm.

TABLE I  
SYSTEM PARAMETERS WITH THEIR DEFAULT VALUES.

Parameter	Value
Number of subcarriers, $M$	256
Number of symbols, $N$	16
Modulation size (QAM)	4
Subcarrier spacing, $\Delta f$	240 kHz
Cyclic prefix size	64
Carrier frequency, $f_c$	30 GHz
SNR	0 dB
Velocity autocorrelation coefficient, $\delta_i$	1.5
Diffusion, $\psi_i$	0.5
Number of targets, $N_T$	4
Number of network nodes, $N_B$	3
Number of antennas per node	1
Time step of the trajectories, $\Delta t$	0.5 sec.
Square region with side length	400 m

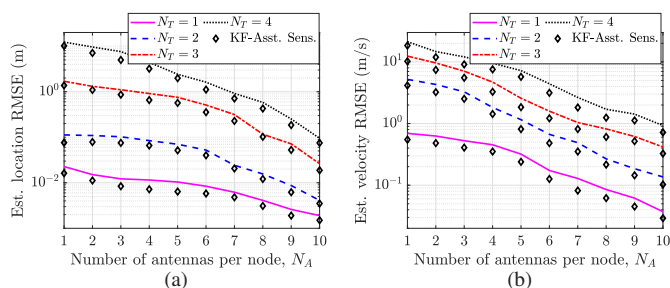


Fig. 4. RMSE improvement with number of antennas per node,  $N_A$  for different numbers of targets,  $N_T$ .

the noises. In Fig. 3(a), RMSE of the estimated locations is measured with SNR. At  $-20$  dB SNR, the performance is significantly better for  $N_T = 1$  target, but, for  $N_T > 1$  targets, the RMSE is increased by around 85 m, because, from (9), in a noisy channel, detection of one peak after the correlation of the two signals in case of a single target is easier than the multiple peaks due to multiple targets. On average, the RMSE increased by 15.53 m, 18.00 m, and 10.03 m for the change in the value of  $N_T$  from 1 to 2, 2 to 3, and 3 to 4, respectively. Further, the KF-assisted active sensing decreases the RMSE on average by 4.96 m. In Fig. 3(b), RMSE for the velocity estimation is determined with SNR for different numbers of targets. Here, on average, the RMSE is increased by 17.50 m/s, 12.29 m/s, and 10.87 m/s for the change in the number of targets,  $N_T$  from 1 to 2, 2 to 3, and 3 to 4. Besides, the KF-assisted sensing decreases the RMSE by 4.02 compared to the active sensing. In Fig. 4, the performance is measured with respect to the number of antennas per node,  $N_A$ . We observe that for any number of targets, the RMSE of the estimated location and velocity decreases with  $N_A$ , because, from Lemma 3, it creates  $N_A^3$  samples which reduces the error by  $N_A^3$ . For  $N_A = 1$ , the average RMSEs in the estimation of location and velocity are 3.53 m and 9.90 m/s, whereas for all  $N_A$  and  $N_T$  values in the plot, the average RMSEs are 1.18 m and 3.44 m/s. Here, the error is decreased by 0.31 m and 0.73 m/s while using the

KF-assisted sensing against the active sensing.

In Fig. 5, we evaluate the performance of the proposed ISAC framework in terms of errors in target localization, velocity estimation, and achievable data rate with variation of the SNR for different values of  $N_A$ , as illustrated in Fig. 5. At an SNR of 0 dB, increasing  $N_A$  from 1 to 10 significantly improves sensing accuracy: the RMSE in estimating the location and velocities of  $N_T = 4$  targets decreases from 24.41 m and 31.65 m/s to 0.23 m and 2.53 m/s, respectively. For comparison, under the same setting in Fig. 4, the use of active sensing further reduces the RMSE from 12.30 m and 21.28 m/s to 0.09 m and 0.93 m/s. These results confirm that active sensing consistently outperforms passive sensing within ISAC, since both the pilot and transmit signals are available to the receiver in the former, whereas in the latter only the pilot is known and the received signal must be iteratively estimated, as described in Algorithm 3. On average, the baseline ISAC scheme yields an RMSE of 25.06 m for location and 31.63 m/s for velocity, while the KF-assisted ISAC improves the accuracy by reducing the errors to 19.76 m and 25.46 m/s, respectively. Furthermore, as shown in Fig. 5(c), the bit error rate (BER) at  $N_A = 1$  is approximately 0.30, which decreases to  $8.13 \times 10^{-2}$  when  $N_A = 4$ . Across the evaluated SNR range, the average BER achieved by ISAC is 0.16, whereas the KF-assisted ISAC achieves a lower BER of 0.13.

Next, Figs. 6 and 7 present a comparative analysis of the different schemes in terms of error improvement for both sensing and communication. In these figures, Act\_Sen\_Rnd and Act\_Sen\_Opt denote the active sensing schemes with receivers deployed randomly and optimally, respectively. The KF\_Act\_Sen\_Opt scheme corresponds to the KF-assisted active sensing with optimally placed receivers. In contrast, ISAC\_Rnd and ISAC\_Opt represent the ISAC schemes under random and optimal receiver deployment, respectively, while KF\_ISAC\_Opt denotes the KF-assisted ISAC scheme with optimally deployed receivers. In Fig. 6, it can be observed that the proposed methods consistently outperform the baseline across all antenna configurations. The reference approach [18] provides moderate improvements, particularly at higher antenna counts, but remains inferior compared to the proposed schemes. Act\_Sen\_Rnd achieves noticeable gains; however, its performance is limited compared to the Act\_Sen\_Opt. KF\_Act\_Sen\_Opt and Act\_Sen\_Opt demonstrate substantial improvements, highlighting the benefit of optimal deployment and temporal correlation exploitation. Similarly, passive sensing in ISAC\_Rnd exhibits only marginal enhancement, whereas the sensing in ISAC\_Opt offers a significant reduction in RMSE. Further performance gains are enhanced by KF\_ISAC\_Opt, particularly as the number of antennas increases. Overall, the results confirm that the combination of antenna optimization and Kalman filtering at optimal deployment of the receivers yields the highest RMSE improvement, thereby establishing its effectiveness for practical multi-antenna sensing systems.

#### A. Numerical Results

To measure the BER performance of the different schemes, we consider 8 dB SNR for the results in Fig. 7. As observed,

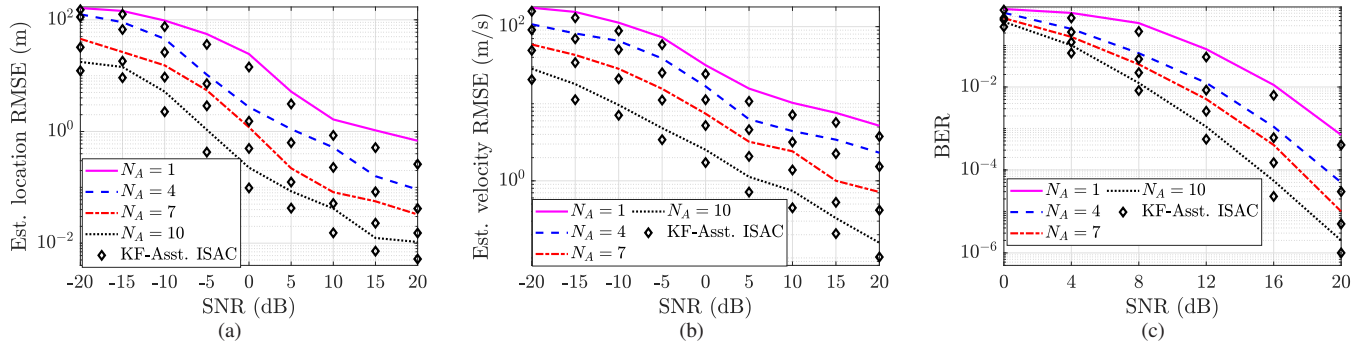


Fig. 5. Performance of ISAC in the localization and the data rate estimation.

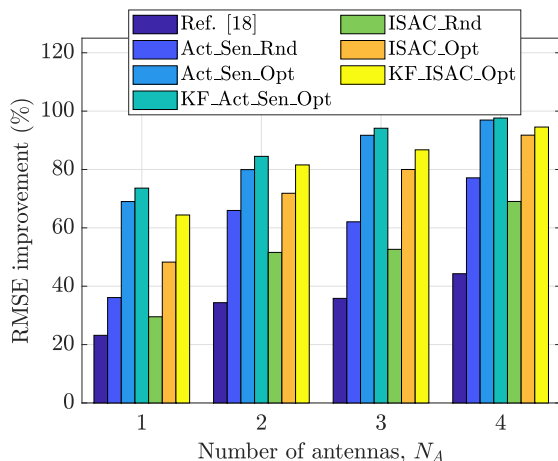


Fig. 6. Performance comparison of different schemes in sensing.

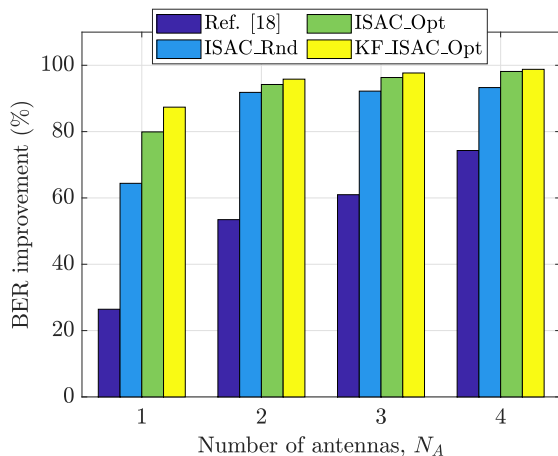


Fig. 7. Performance comparison of different schemes in communication.

the proposed KF\_ISAC\_Opt scheme consistently achieves the highest improvement across all antenna configurations when compared to the scheme in [18]. For  $N_A = 1$ , [18] reports a BER of 1.7284, whereas ISAC\_Rnd, ISAC\_Opt, and KF\_ISAC\_Opt reduce it significantly to 0.6152, 0.3472, and 0.2182, respectively, corresponding to improvements of 64.41%, 79.91%, and 87.37%. At  $N_A = 4$ , [18] achieves a BER of 0.6725, while ISAC\_Rnd, ISAC\_Opt,

and KF\_ISAC\_Opt further reduce it to 0.0920, 0.0652, and 0.0471, achieving 93.96%, 98.14%, and 98.78% improvements, respectively. Notably, as the number of antennas increases, the relative improvement margin between KF\_ISAC\_Opt and other schemes becomes more prominent, underlining its scalability advantage. The improvement of ISAC\_Rnd remains comparatively modest, especially at lower antenna numbers, due to its randomized nature, whereas ISAC\_Opt provides competitive performance but still lags behind the KF\_ISAC\_Opt. Overall, these results confirm that the KF\_ISAC\_Opt offers a significant advantage in reducing BER, particularly in multi-antenna systems.

#### APPENDIX A TRAJECTORIES GENERATION

For the obtained numerical results in Section V, the trajectories of the randomly moving vehicles are generated using the Algorithm A.1 as described below.

**Algorithm A.1.** Trajectory generation of a randomly moving  $i$ th vehicle/target.

**Require:** Number of time steps  $N_{ts} = 20$ , time step  $\Delta t = 0.5$  s, acceleration noise standard deviation  $\sigma_a = 0.5$  m/s<sup>2</sup>, jerk noise standard deviation  $\sigma_j = 0.2$  m/s<sup>2</sup>, heading Gaussian noise standard deviation  $\sigma_\theta = \pi/45$  rad, sudden turn probability  $p_t = 0.1$ , sudden turn Gaussian noise standard deviation  $\sigma_s = \pi/6$  rad, side length  $L = 400$  m of the sq. bounded region

**Ensure:** Location X, Y coordinates  $\alpha_i, \beta_i \in \mathbb{R}^{N_{ts}}$  and velocity X, Y coordinates  $\mathbf{v}_{i,x}, \mathbf{v}_{i,y} \in \mathbb{R}^{N_{ts}}$  of the  $i$ th vehicle

- 1: Randomly initialize location  $(\alpha_{i,1}, \beta_{i,1})$  in the square region, speed  $s_i \in (10, 15)$  m/s, and heading angle  $\theta_{i,1} \in (0, 2\pi)$ . Set initial acceleration  $a_{i,1} = 0$  m/s<sup>2</sup>.
- 2: Obtain  $v_{i,x,1} = s_{i,1} \cos(\theta_{i,1})$  and  $v_{i,y,1} = s_{i,1} \sin(\theta_{i,1})$
- 3: **for**  $t = 2$  to  $N_{ts}$  **do**
- 4:     Add Gaussian random jerk in the acceleration:  $a_{i,t} = a_{i,t-1} + \mathcal{N}(0, \sigma_j)$  such that  $a_{i,t} \in [-2, 2]$  m/s<sup>2</sup>
- 5:     Update speed:  $s_{i,t} = s_{i,t-1} + a_{i,t} \Delta t$  such that  $s_{i,t} \in [5, 20]$  m/s
- 6:     **if** sudden turn occurs with probability  $p_t$  **then**
- 7:         Sudden turn:  $\theta_{i,t} = \theta_{i,t-1} + \mathcal{N}(0, \sigma_s)$
- 8:     **else**
- 9:         Small turn:  $\theta_{i,t} = \theta_{i,t-1} + \mathcal{N}(0, \sigma_\theta)$
- 10:    **end if**

- 11: Determine velocity components:  $v_{i,x,t} = s_{i,t} \cos(\theta_{i,t})$   
and  $v_{i,y,t} = s_{i,t} \sin(\theta_{i,t})$
- 12: Update location components:  $\alpha_{i,t} = \alpha_{i,t-1} + v_{i,x,t} \Delta t$   
and  $\beta_{i,t} = \beta_{i,t-1} + v_{i,y,t} \Delta t$  such that  $\alpha_{i,t}, \beta_{i,t} \in \{0, L\}$
- 13: **end for**
- 

- [21] D. S. Johnson, J. M. London, M.-A. Lea, and J. W. Durban, "Continuous-time correlated random walk model for animal telemetry data," *Ecology*, vol. 89, no. 5, pp. 1208–1215, 2008.
- [22] G. A. Terejanu, "Extended kalman filter tutorial," *University at Buffalo*, vol. 27, p. 6, 2008.

## REFERENCES

- [1] F. Liu, C. Masouros, A. P. Petropulu, H. Griffiths, and L. Hanzo, "Joint radar and communication design: Applications, state-of-the-art, and the road ahead," *IEEE Transactions on Communications*, vol. 68, no. 6, pp. 3834–3862, 2020.
- [2] R. Hadani, S. Rakib, M. Tsatsanis, A. Monk, A. J. Goldsmith, A. F. Molisch, and R. Calderbank, "Orthogonal time frequency space modulation," in *2017 IEEE Wireless Communications and Networking Conference (WCNC)*, 2017, pp. 1–6.
- [3] W. Yuan, Z. Wei, S. Li, R. Schober, and G. Caire, "Orthogonal time frequency space modulation—part iii: Isac and potential applications," *IEEE Communications Letters*, vol. 27, no. 1, pp. 14–18, 2023.
- [4] K. Han, K. Meng, X.-Y. Wang, and C. Masouros, "Network-level isac design: State-of-the-art, challenges, and opportunities," *arXiv preprint arXiv:2505.01295*, 2025.
- [5] T. Su, Z. Zhang, J. Chu, R. Zhao, and Y. Huang, "Joint doa and toa estimation for moving mimo radar based on ofdm-isac signals," *IEEE Transactions on Vehicular Technology*, 2025.
- [6] N. Decarli, S. Bartoletti, A. Bazzi, R. A. Stirling-Gallacher, and B. M. Masini, "Performance characterization of joint communication and sensing with beyond 5g nr-v2x sidelink," *IEEE Transactions on Vehicular Technology*, vol. 73, no. 7, pp. 10 044–10 059, 2024.
- [7] Y. Zhuo and Z. Wang, "Performance analysis of isac system under correlated communication-sensing channel," *IEEE Transactions on Vehicular Technology*, vol. 72, no. 12, pp. 16 823–16 827, 2023.
- [8] X. Cheng, D. Duan, S. Gao, and L. Yang, "Integrated sensing and communications (isac) for vehicular communication networks (vcn)," *IEEE Internet of Things Journal*, vol. 9, no. 23, pp. 23 441–23 451, 2022.
- [9] Y. Li, Z. Wei, Y. Wang, H. Liu, and Z. Feng, "Cooperative sensing in uplink isac system: A multi-user waveform optimization approach," *IEEE Transactions on Vehicular Technology*, 2025.
- [10] Q. Zhang, H. Sun, X. Gao, X. Wang, and Z. Feng, "Time-division isac enabled connected automated vehicles cooperation algorithm design and performance evaluation," *IEEE Journal on Selected Areas in Communications*, vol. 40, no. 7, pp. 2206–2218, 2022.
- [11] Z. Hong, S. Sugiura, C. Xu, and L. Hanzo, "Cooperative isac networks: Performance analysis, scaling laws and optimization," *IEEE Transactions on Wireless Communications*, 2024.
- [12] K. Meng and C. Masouros, "Cooperative sensing and communication for isac networks: Performance analysis and optimization," in *2024 IEEE 25th International Workshop on Signal Processing Advances in Wireless Communications (SPAWC)*. IEEE, 2024, pp. 446–450.
- [13] B. Yin, J. Jia, Y. Liu, J. Chen, and X. Wang, "Cooperative isac: A mutual information-based approach for the two-base stations case," *IEEE Transactions on Vehicular Technology*, 2025.
- [14] W. Yuan, Z. Wei, S. Li, R. Schober, and G. Caire, "Orthogonal time frequency space modulation—part iii: Isac and potential applications," *IEEE Communications Letters*, vol. 27, no. 1, pp. 14–18, 2022.
- [15] J. Wu, W. Yuan, Z. Wei, J. Yan, and D. W. K. Ng, "Optimal ber minimum precoder design for ofts-based isac systems," in *ICASSP 2024-2024 IEEE International Conference on Acoustics, Speech and Signal Processing (ICASSP)*. IEEE, 2024, pp. 12 966–12 970.
- [16] O. Zacharia and M. V. Devi, "Fractional delay and doppler estimation for ofts based isac systems," in *2023 IEEE Wireless Communications and Networking Conference (WCNC)*. IEEE, 2023, pp. 1–6.
- [17] Y. Fan, S. Wu, X. Bi, and G. Li, "Power allocation for cell-free massive mimo isac systems with ofts signal," *IEEE Internet of Things Journal*, 2024.
- [18] S. Sruti, A. A. Kumar, and K. Giridhar, "Joint association and localization of multiple targets in an ofts-based multistatic isac system," *IEEE Transactions on Aerospace and Electronic Systems*, 2025.
- [19] J. Wu, W. Yuan, Z. Wei, J. Yan, and D. W. K. Ng, "Optimal ber minimum precoder design for ofts-based isac systems," in *ICASSP 2024-2024 IEEE International Conference on Acoustics, Speech and Signal Processing (ICASSP)*. IEEE, 2024, pp. 12 966–12 970.
- [20] P. Raviteja, Y. Hong, E. Viterbo, and E. Biglieri, "Practical pulse-shaping waveforms for reduced-cyclic-prefix ofts," *IEEE Transactions on Vehicular Technology*, vol. 68, no. 1, pp. 957–961, 2018.